









Evaluation of Recent Measurements of Mercury’s Moments of Inertia and Tides Using a Comprehensive Markov Chain Monte Carlo Method

Sander Goossens^{1,2,3,7} , Joe P. Renaud^{2,4} , Wade G. Henning^{2,3,5} , Erwan Mazarico² , Stefano Bertone^{1,2,3} , and Antonio Genova⁶ 

¹ Center for Space Sciences and Technology, University of Maryland, Baltimore County, Baltimore, Maryland, USA; sander.j.goossens@nasa.gov

² NASA Goddard Space Flight Center, Greenbelt, Maryland, USA

³ Center for Research and Exploration in Space Science and Technology (CRESTT) II, NASA/GSFC, Greenbelt, Maryland, USA

⁴ Universities Space Research Association, Columbia, Maryland, USA

⁵ University of Maryland, College Park, Department of Astronomy, College Park, Maryland, USA

⁶ Sapienza, University of Rome, Department of Mechanical and Aerospace Engineering, Rome, Italy

Received 2021 August 18; revised 2021 December 21; accepted 2022 January 5; published 2022 February 11

Abstract

Recent estimates of Mercury’s rotational state yield different obliquity values, resulting in normalized polar moment of inertia values of either 0.333 or 0.346. In addition, recent measurements of Mercury’s tidal response, as expressed by its Love number k_2 , are higher than previously reported. These different measurements have implications for our understanding of Mercury’s interior structure. We perform a comprehensive analysis of models of Mercury’s interior structure using a Markov Chain Monte Carlo approach, where we explore models that satisfy the various measurements of moments of inertia and mean density. In addition, we explore models that either have Mercury’s tidal response as a measurement or predict its tidal response. We find that models that match the lower polar moment value also fit or predict the recent, higher Love number. Models that match the higher polar moments predict Love numbers even higher than current estimates. For the resulting interior structure models, we find a wide range of viscosities at the core–mantle boundary, including low values that could be consistent with the presence of partial melt, with higher viscosities also equally allowed in our models. Despite the possibility of low viscosities, our results do not show a preference for particularly high temperatures at the core–mantle boundary. Our results include predicted values for the pressure and temperature of Mercury’s core, and the displacement Love numbers.

Unified Astronomy Thesaurus concepts: Planetary interior (1248); Planetary structure (1256); Mercury (planet) (1024); Markov chain Monte Carlo (1889); Tides (1702)

Supporting material: figure set

1. Introduction

Mercury can be considered an end member of formation processes in the solar system, in both a dynamic and a compositional sense, because of its location and high average density (e.g., Chapman 1988). Knowledge of Mercury’s interior structure is thus of paramount importance to better understand the formation and evolution of the solar system. The Mariner 10 flybys in 1974 and 1975 (e.g., Dunne 1974) provided us with the first close-up views of the planet, the first clues about its interior, with the discovery of its magnetic field (Ness et al. 1974), and the first measurements of its gravitational field (Anderson et al. 1987). The next visit to the innermost planet did not occur until 2008, when NASA’s MErcury Surface, Space ENvironment, GEochemistry, and Ranging (MESSENGER) spacecraft performed its first Mercury flyby, which was followed by its insertion into a highly eccentric orbit around Mercury in 2011. It carried seven instruments and a radio science investigation, with the goal of answering questions about Mercury’s formation,

geologic history, magnetic field, core, polar areas, and exosphere (Solomon et al. 2007).

The quantities that we use to probe the planet’s interior are moments of inertia, which depend on the radial density distribution inside the planet. Peale (1976) showed that the state of Mercury’s core can be derived from the values of its polar moment of inertia for the entire planet C and its crust–mantle polar moment C_m , which are themselves determined by measuring several quantities concerning Mercury’s gravity field and rotational state: (1) Mercury’s second-degree gravitational harmonics; (2) the planet’s obliquity (the axial tilt of a planet); and (3) the amplitude of its longitudinal librations (the longitudinal oscillations in the planet’s spin rate), forced at the 88 day orbital period. This is possible because Mercury is assumed to be in, or close to, an equilibrium Cassini state, where its spin axis, its orbit normal, and the normal to the invariable plane are coplanar (e.g., Colombo 1966; Peale 1969). Peale (1976) and Peale et al. (2002) showed how to relate the gravity and rotational quantities to the entire polar and crust–mantle polar moments. The polar moment is computed as the mass distribution of the entire planet around the z -axis, which is assumed to be aligned with the rotation axis. We refer to the entire polar moment simply as the polar moment, and it is denoted by C . The crust–mantle polar moment comprises the solid outer shell, and is expressed as the ratio between the polar moment of the crust and mantle and the entire polar moment, and hence becomes C_m/C . The entire polar moment is also

⁷ Currently at: Planetary Geology, Geophysics, and Geochemistry Laboratory, NASA Goddard Space Flight Center, Greenbelt, Maryland, USA.



Table 1
Values for Mercury’s Rotation Parameters, Moments of Inertia, and Love Numbers from Various Studies

Reference	Forced Libration Angle (arcsec)	Obliquity (arcmin)	$C/(MR^2)$ (no unit)	C_m/C (no unit)	Liquid Core Size (km)	Love Number (no unit)
Margot et al. (2007) ^a	35.8 ± 2	2.11 ± 0.1
Smith et al. (2012) ^b	...	2.06 ± 0.1	0.353 ± 0.017	0.452 ± 0.035	2030 ± 37	...
Margot et al. (2012) ^c	38.5 ± 1.6	2.04 ± 0.08	0.346 ± 0.014	0.431 ± 0.025	1998	...
Mazarico et al. (2014) ^d	...	2.06 ± 0.16	0.349 ± 0.014	0.424 ± 0.024	2020 ± 30	$k_2 = 0.451 \pm 0.014$
Stark et al. (2015) ^e	38.9 ± 1.3	2.029 ± 0.085	0.346 ± 0.011	0.421 ± 0.0214
Genova et al. (2019) ^f	40.0 ± 8.7	1.968 ± 0.027	0.333 ± 0.005	0.443 ± 0.019	1967 ± 23	$k_2 = 0.569 \pm 0.025$
Konopliv et al. (2020) ^g	...	1.99 ± 0.12	0.337 ± 0.02	0.438 ± 0.03	...	$k_2 = 0.53 \pm 0.03$
	...	2.04 ± 0.1	0.345 ± 0.02
Bertone et al. (2021) ^h	39.03 ± 1.1	2.031 ± 0.03	0.343 ± 0.006	0.423 ± 0.012	2020 ± 50	$h_2 = 1.55 \pm 0.65$

Notes.

^a Precise gravity not yet available.

^b Forced librations from Margot et al. (2007) and a revised obliquity from Margot et al. (2011).

^c Used gravity results from Smith et al. (2012). Core size from a two-layer constant density model. An error estimate for the core size was not provided.

^d Forced librations not estimated, but used Margot et al. (2012). Core size from Hauck et al. (2013).

^e Used laser altimeter data for rotational parameters; gravity from Mazarico et al. (2014).

^f Estimated forced librations, but used Margot et al. (2012) values.

^g No moments of inertia given; the values here are inferred from obliquity, and the forced librations are from Margot et al. (2012). Because of the discrepancy between obliquity and pole coordinates (see the text), we list two different polar moment values.

^h Analysis is based on altimetric crossovers. Gravity was not estimated.

often normalized as $C/(MR^2)$, with M being the mass of the entire planet and R being the radius of the planet.

In Table 1, we present key measurements of Mercury’s rotation and derived values for these moments from various recent studies. We also include estimated values of Love numbers: the parameter k_2 (which is dimensionless) describes how the gravitational potential field of a self-gravitating planetary body changes in response to the second-order spherical harmonic terms of the gravitational field of another object, in this case the Sun. The quantity h_2 (also dimensionless) describes the vertical surface displacement, and it is also included in Table 1.

Earth-based radar observations characterized Mercury’s liquid core for the first time by providing measurements of its forced librations at the 88 day period and of its obliquity (Margot et al. 2007). MESSENGER provided the first comprehensive measurements of Mercury’s gravitational field (Smith et al. 2012) needed to complement the rotation observations in order to be able to apply the formalism of Peale et al. (2002). This yielded the first moment of inertia estimates of $C/(MR^2) = 0.353 \pm 0.017$ and $C_m/C = 0.452 \pm 0.035$ (Smith et al. 2012). A Monte Carlo analysis indicated a liquid core radius of 2030 ± 37 km, and a density of the solid outer shell of 3650 ± 225 kg m⁻³. The latter was higher than expected, because of the relatively high value for C_m/C , and a solid FeS layer on top of a liquid FeS layer at the top of the core was invoked to match this density. Using additional Earth-based radar measurements, Margot et al. (2012) provided updated values for Mercury’s forced libration and obliquity angles. Together with MESSENGER results, they provided updated estimates for Mercury’s moments of inertia of $C/(MR^2) = 0.346 \pm 0.014$ and $C_m/C = 0.431 \pm 0.025$. These were used by Hauck et al. (2013) to provide refined estimates of Mercury’s interior structure: the liquid core radius was found to be 2020 ± 30 km, with a density below the core–mantle boundary (CMB) of 6980 ± 280 kg m⁻³, and a density just above the core of 3380 ± 200 kg m⁻³. With this core density, it was concluded that Mercury must have a significant amount of light elements such as S and/or Si in the

core, which is also required to maintain the core in a partially molten state. Similar results were obtained by Rivoldini & van Hoolst (2013), who also noted that the geodesy data, because of relatively large error bars, could not distinguish between models with a fully liquid core and models with a solid inner core included.

The MESSENGER mission had several extended mission phases where the spacecraft’s orbital altitude and the latitude of its pericenter changed. Using three years of MESSENGER data, Mazarico et al. (2014) provided an updated model of Mercury’s gravity field and its obliquity, as well as the first estimate of its potential Love number of degree 2 ($k_2 = 0.451 \pm 0.014$). Mazarico et al. (2014) also tested the estimation of the forced libration angle of Mercury, but found the radio data not sensitive enough. Their results were later confirmed through a separate analysis by Verma & Margot (2016), although this obliquity solution is very different from, and only marginally consistent with, that of Mazarico et al. (2014). The updated values for the moments of inertia from Mazarico et al. (2014) were $C/(MR^2) = 0.349 \pm 0.014$ and $C_m/C = 0.424 \pm 0.024$. With these values, Knibbe & van Westrenen (2015) performed additional interior modeling. They explored models of different composition, and also used large new values for Mercury’s contraction in time due to global cooling (Byrne et al. 2014) as an additional constraint. They found a liquid core radius between 1985 and 2090 km, and an inner core radius smaller than 1454 or 1543 km, for cores rich in S or Si, respectively. They also found the suggested solid FeS layer to be unlikely, because the solid part would be denser than the liquid part underneath. In addition, improved obliquity values decreased the initial $C/(MR^2)$ and C_m/C values from Smith et al. (2012), reducing the density of the solid shell (the crust and mantle, and the solid FeS layer, if taken into account). Recent results using MESSENGER’s X-Ray Spectrometer measurements of Ti/Si also argue against the FeS layer, from a geochemical point of view (Cartier et al. 2020). Given the measurement of Mercury’s k_2 , Padovan et al. (2014) and Steinbrügge et al. (2018a) investigated Mercury’s

tidal response. In addition, Stark et al. (2015) updated Mercury’s rotational state using data from the Mercury Laser Altimeter (MLA) instrument (Cavanaugh et al. 2007). They found values for the moments of inertia of $C/(MR^2) = 0.346 \pm 0.011$ and $C_m/C = 0.421 \pm 0.0214$.

In the final year of its mission, the Sun’s gravity lowered MESSENGER’s orbit down to altitudes around 25 km above the surface. This greatly increased sensitivity with respect to the gravity field, and Genova et al. (2019) provided the first gravity field model using the entire data set. This analysis was based on co-estimating Mercury’s orbit, its gravity field, rotational parameters, and MESSENGER’s orbit (Genova et al. 2018). Their obliquity estimate unambiguously satisfies the Cassini state, where other estimates show an offset but are statistically consistent with the Cassini state. Genova et al. (2019) found a lower obliquity than previously reported, which resulted in a lower polar moment of inertia, with $C/(MR^2) = 0.333 \pm 0.005$ and $C_m/C = 0.443 \pm 0.019$. From this lower moment of inertia, and its improved error, they showed that Mercury likely has a solid inner core. They found that the radius of the liquid core is much smaller than previous analysis indicated, at 1967 ± 23 km for a model with an FeSi core. They also provided an updated estimate of $k_2 = 0.569 \pm 0.025$, larger than the previous estimate.

Additional analysis of MESSENGER tracking data by Konopliv et al. (2020) yielded a similar reported estimate of the obliquity, although it should be noted that Steinbrügge et al. (2021) pointed out that the reported obliquity is not consistent with the reported R.A. and decl. of the pole. If the reported pole coordinates are used, an obliquity much closer to that of Margot et al. (2012) is found, which means that the polar moment of inertia is 0.345 instead of 0.337. Konopliv et al. (2020) also provided an estimate of $k_2 = 0.53 \pm 0.03$, consistent with the higher value of Genova et al. (2019). Recent analysis of MLA altimetric crossovers (Bertone et al. 2021) yielded an additional measurement of Mercury’s obliquity that is fully consistent with the Cassini state, but this value is higher than that of Genova et al. (2019), resulting in a higher polar moment of inertia of $C/(MR^2) = 0.343 \pm 0.006$, and in a value of $C_m/C = 0.423 \pm 0.012$ (using the degree 2 coefficients from Genova et al. 2019). Multiple combinations of the R.A. and decl. of the pole can satisfy the Cassini state requirement, as can be seen in, for example, Bertone et al. (2021; Figure A1), resulting in different obliquities, and hence the discrepancy where two different obliquities satisfy the Cassini state.

These discrepancies in obliquity are intriguing, especially since two recent results (Genova et al. 2019; Bertone et al. 2021) place Mercury in very close agreement with the Cassini state. It should be noted that neither study constrains the solution to do so. Both studies use different techniques and data, with the Genova et al. (2019) study using radio science data and the Bertone et al. (2021) study using altimetry data. Both studies have similar errors on the obliquity (see Table 1). This could indicate a difference between the orientation of the gravity field, as obtained from the radio data (which can be considered as a quantity describing the entire planet, as it is related to the gravity field), and that of the outer layers. This has already been suggested by Verma & Margot (2016), and the possibility is also raised by Bertone et al. (2021). The existence of a solid inner core itself can also influence the Cassini state (Peale et al. 2016; Baland et al. 2017; Dumberry 2021), yet the effects may be small, below the

current error levels. It is outside the scope of this analysis to try and resolve this discrepancy.

Yet, clearly, the different moments of inertia have a large effect on the determination of the parameters of Mercury’s interior structure, most notably the size of the liquid core (see Table 1). Steinbrügge et al. (2021) recently investigated interior models of Mercury using these different moment of inertia values. They computed models that match Mercury’s mean density, its polar moment of inertia, and the amplitude of its forced librations at the 88 day period. In their analysis, the models that satisfy the lower polar moment of inertia pose several challenges: they find a relatively large inner core, a relatively high temperature at the CMB, low viscosities at this boundary, and a low mantle density. They also indicate that the low viscosities required to match k_2 imply a significantly weaker mantle.

Here, we investigate the different moments of inertia and their influence on the interior structure parameters with a different approach to that of Steinbrügge et al. (2021). Their strategy was to investigate models that match the specific moment of inertia values, and they explicitly stated that they would not conduct a probability analysis. Yet they did indicate that when they took into account the error on the forced librations, some of the issues that they found with the lower polar moment were alleviated. In contrast, we use a Markov Chain Monte Carlo (MCMC) approach (e.g., Mosegaard & Tarantola 1995), where we include k_2 as an additional observation, together with Mercury’s mean density and its polar and crust–mantle polar moments of inertia. This allows us to explore models consistent with these observations and their quoted errors, by mapping the range of allowed values of the estimated parameters that match the measurement within their given errors. We believe that this provides a more complete picture of the distributions of possible interior structure models than focusing on models that match the central values. In addition, we also explore models that only satisfy the moments of inertia and the planet’s average density, where we predict the k_2 for those likely structures. This allows us to probe for any inconsistencies between the models and measurements.

This paper is structured as follows. In Section 2, we introduce our modeling and assumptions. We then show the results for various different cases and measurements in Section 3. We discuss these results and how they compare to other studies in Section 4. We end with our conclusions in Section 5.

2. Interior Structure Modeling

In this section, we describe our modeling method. We first explain how we construct self-consistent models for Mercury’s interior structure. We use the obtained structure to compute its tidal response. We then combine these inputs in an MCMC method to determine the a posteriori probability density functions of the parameters that describe the interior structure model.

2.1. Self-consistent Interior Structure Models

Our interior structure modeling follows the exact same approach as presented in Genova et al. (2019), which was itself based on earlier works (Hauck et al. 2007, 2013; Knibbe & van Westrenen 2015). We assume a spherically symmetric planet in hydrostatic equilibrium, where the density ρ varies only with

the radius r in the planet. The differential equation for the local pressure P in the planet as a function of density and local gravitational acceleration g is given by (e.g., Turcotte & Schubert 2002; Sohl & Schubert 2015)

$$\frac{dP(r)}{dr} = -\rho(r)g(r), \quad (1)$$

where we indicate which parameters are functions of r . The cumulative mass $M(r)$ is defined as the integral over the cumulative volume,

$$V(r) = \frac{4}{3}\pi r^3, \quad (2)$$

so that

$$M(r) = \int_0^r \rho(r')dV(r') = 4\pi \int_0^r \rho(r')r'^2 dr', \quad (3)$$

or, in differential equation form,

$$\frac{dM(r)}{dr} = 4\pi r^2 \rho(r). \quad (4)$$

Finally, the local gravitational acceleration can be derived from

$$g(r) = \frac{GM(r)}{r^2} = \frac{4\pi G}{r^2} \int_0^r \rho(r')r'^2 dr', \quad (5)$$

where G is the universal gravitational constant. In differential equation form, this reads

$$\frac{dg(r)}{dr} = 4\pi G\rho(r) - \frac{2g(r)}{r}. \quad (6)$$

This gives a set of equations that can be integrated to give $P(r)$.

In general, however, the density is dependent on both pressure and temperature, so that an equation of state (EOS) relating these three, and a temperature profile, are required. Following Hauck et al. (2013) and Knibbe & van Westrenen (2015), we use the third-order Birch–Murnaghan EOS

$$P = \frac{3K_0}{2} \left[\left(\frac{\rho}{\rho_0} \right)^{\frac{7}{3}} - \left(\frac{\rho}{\rho_0} \right)^{\frac{5}{3}} \right] \times \left[1 + \frac{3}{4}(K'_0 - 4) \left(\left(\frac{\rho}{\rho_0} \right)^{\frac{2}{3}} - 1 \right) \right] + \alpha_0 K_0 (T - T_0), \quad (7)$$

where K_0 and K'_0 are the isothermal bulk modulus and its pressure derivative, ρ_0 is the reference density, α_0 is the reference volumetric coefficient of thermal expansion, and T and T_0 are the local temperature and reference temperature, respectively. We list the values for these parameters in Table 2. For the temperature profile, we follow earlier works (Hauck et al. 2007, 2013; Rivoldini & van Hoolst 2013; Knibbe & van Westrenen 2015) and assume an adiabatic profile within the liquid part of the core, resulting in

$$\frac{dT}{dP} = \frac{\alpha T}{\rho C_P}, \quad (8)$$

with C_P being the specific heat capacity at constant pressure. The coefficient of thermal expansion α can be found from

$$\alpha_0 K_0 = \alpha K, \quad (9)$$

knowing that the equation for the bulk modulus K is given by

$$K = \rho \frac{dP}{d\rho}. \quad (10)$$

We assume an isothermal temperature for the solid inner core, following earlier studies (Hauck et al. 2007, 2013; Knibbe & van Westrenen 2015; Steinbrügge et al. 2021), and considering that the moment of inertia is not very sensitive to the thermal state of the inner core (Rivoldini et al. 2009; Rivoldini & van Hoolst 2013). We obtain the inner core temperature in the following way: Equations (8)–(10) are integrated from the CMB radius toward the center. When the inner core boundary (ICB) is reached, the temperature remains constant, which is then the inner core temperature, T_{ICB} . The boundary condition for the temperature profile is given by the temperature T_{CMB} at the CMB, which is a free parameter in our analysis (see Section 2.3).

For the crust and mantle, we assume (separate) constant densities, and thus no EOS or temperature profiles are necessary. This is reasonable given the low-pressure regime (~ 5 GPa) and relatively small thickness of both Mercury’s crust and mantle. Temperature changes in the thin mantle only affect the density profile by a small amount (Hauck et al. 2013; Knibbe & van Westrenen 2015). For the computation of the tidal response, however, we will specify a temperature profile (see Section 2.2), due to the high sensitivity of tides to viscosity as a proxy for temperature.

In our modeling, the solid inner core radius is a parameter, which could lead to thermodynamical inconsistencies, such as enforcing a solid phase, while local pressure and temperature might not allow this, for a given composition. We enforce density discontinuities at the boundaries (by rejecting models that do not have such an increase), which should mitigate this effect. We also deem our parameter space wide enough (see Section 2.3) to cover most configurations. This choice is similar to earlier works by Hauck et al. (2013) and Knibbe & van Westrenen (2015). The latter indicate that while temperature inconsistencies can be large, the resulting density inconsistencies are on the order of 2.5%, which is about the same order of magnitude as the effect of the uncertainties in the parameters for the EOS. Such an error can be accommodated by subtle changes in related parameters as a result of our MCMC analysis without affecting the resulting parameter distributions significantly. In Section 4.3, we discuss determining the liquid–solid boundary from local conditions, and the effects on our results in more detail.

In order to solve the EOS, we first need to specify the composition of the core, since this will determine the values of the various material coefficients. While Genova et al. (2019) explored different models with different light elements in the core and with different layering, here we focus on Mercury models that only have Si as the light element in the core. While the core can also contain S as a light element (for example, Tao & Fei 2021 studied the Fe–Si–S system, and showed that Si preferentially partitions in the inner core, whereas S remains in the liquid outer core; and a recent analysis by Knibbe et al. 2021 considered C as an addition to Si), it at least contains Si (Chabot et al. 2014), and S may not even be a required element (Knibbe & van Westrenen 2018). We do not consider additional layers, such as the solid FeS top layer to the core suggested by Smith et al. (2012), but later deemed unnecessary

Table 2
Equation of State Parameters Used to Model the FeSi Core

Parameter	Value	Unit	Reference
FeSi liquid (17 wt% Si)			
Bulk modulus K_0	73	GPa	
Bulk modulus pressure derivative K'_0	4.0	...	
Reference density ρ_0	6000	kg m^{-3}	Sanloup et al. (2004); Yu & Secco (2008)
Coefficient of thermal expansion α_0	9.2×10^{-5}	K^{-1}	
Reference temperature T_0	1723	K	
FeSi solid (17 wt% Si)			
Bulk modulus K_0	199	GPa	Lin et al. (2003)
Bulk modulus pressure derivative K'_0	5.66	...	
Reference density ρ_0	7147	kg m^{-3}	
Coefficient of thermal expansion α_0	6.4×10^{-5}	K^{-1}	
Reference temperature T_0	300	K	
Fe liquid			
Bulk modulus K_0	87	GPa	
Bulk modulus pressure derivative K'_0	5.0	...	
Reference density ρ_0	7019	kg m^{-3}	Anderson & Ahrens (1994); Balog et al. (2003)
Coefficient of thermal expansion α_0	9.2×10^{-5}	K^{-1}	
Reference temperature T_0	1770	K	
Fe solid			
Bulk modulus K_0	165	GPa	
Bulk modulus pressure derivative K'_0	5.5	...	
Reference density ρ_0	8170	kg m^{-3}	Komabayashi & Fei (2010)
Coefficient of thermal expansion α_0	6.4×10^{-5}	K^{-1}	
Reference temperature T_0	293	K	
Additional parameter (used for all materials above)			
Specific heat capacity C_p	825	$\text{J K}^{-1} \text{kg}^{-1}$	Beutl et al. (1994)

by Knibbe & van Westrenen (2015) and subsequent papers, so that our Mercury models consist of a solid FeSi inner core, a liquid FeSi outer core, a mantle, and a crust. The core composition is then specified by the fraction of the element Si. In order to specify the EOS parameters for a given weight fraction of Si, we linearly interpolate (and extrapolate) between values for pure iron and values for FeSi with 17 wt% Si, for both the liquid and solid phases, following Knibbe & van Westrenen (2015).

The Si weight fractions for the solid and liquid parts of the core are often taken to be the same (Hauck et al. 2013; Knibbe & van Westrenen 2015), because experiments have demonstrated that, at a pressure of 21 GPa, a solid precipitate from a liquid Fe–FeSi alloy has the same composition as that alloy (Kuwayama & Hirose 2004). However, possible compositional contrasts between the solid and liquid layers have also been noted (Fischer et al. 2014). While this may occur at pressures much higher than in Mercury’s core, we leave open the option of having different weight fractions.

In Table 2, we list the EOS parameters that we used for FeSi. We solve the EOS using a Levenberg–Marquardt method that we implemented using the freely available MINPACK software library (More et al. 1984). The set of equations describing the interior structure is iteratively integrated, starting with the boundary condition that the pressure at the planet’s surface (we assume a radius of 2440 km for Mercury) is zero. We iterate the integration to ensure that the gravitational acceleration at the

center of the planet is zero. For the numerical integration, we divide the planet into layers of 1 km in thickness.

Once we have computed a consistent structure from a set of starting parameters (such as the radii for the inner and outer core, the thickness of the crust, and several others that we will discuss in Section 2.3), we can compute the polar moment of inertia from (Turcotte & Schubert 2002)

$$C = \frac{8\pi}{3} \int_0^R \rho r'^4 dr'. \quad (11)$$

For the crust–mantle polar moment C_m , the integration starts at the CMB. With the mass for the model also computed, we can readily compute $C/(MR^2)$ and also C_m/C . These can then be compared to the measured quantities.

2.2. Viscoelastic Tidal Deformation Modeling

A world that is viscoelastic will express a complex-valued \bar{k}_2 . The real portion describes the ratio between the unperturbed and perturbed gravitational potential, while the imaginary portion quantifies the planet’s ability to dissipate energy into its interior via tidal friction. This latter value is often described by a geometric phase lag between where a tidal bulge is pointing and where it would be pointing if it were perfectly elastic. For Mercury, we currently cannot discern observationally between the real and imaginary parts, so for the purposes of this paper we will use the term k_2 to signify $|\bar{k}_2|$, which is approximately equal to $\Re[\bar{k}_2]$.

Table 3
Andrade and Sundberg–Cooper Rheological Laws and Parameter Values

Rheological Law	Complex Shear Modulus $\bar{\mu}$ Expression ^a				
Andrade	$\frac{\mu s}{s + \frac{\mu}{\eta} + s\mu^\alpha \alpha! (s\eta\zeta)^{-\alpha}}$				
Sundberg–Cooper	$\frac{\mu s \left(\frac{\mu'}{\eta'} + s \right)}{s^2 (1 + \mu^\alpha \alpha! (s\eta\zeta)^{-\alpha}) + s \left(\frac{\mu}{\eta} + \frac{\mu + \mu'}{\eta'} + \frac{\mu'}{\eta'} \mu^\alpha \alpha! (s\eta\zeta)^{-\alpha} \right) + \frac{\mu\mu'}{\eta\eta'}}$				
Parameter	Symbol	Value	Unit	Reference	
Shear rigidity	μ	varies	GPa	...	
Shear rigidity defect ^b	μ'	5μ	GPa	Henning et al. (2009); Renaud & Henning (2018)	
Viscosity	η	varies	Pa s	...	
Voigt–Kelvin viscosity	η'	0.02η	Pa s	Henning et al. (2009); Renaud & Henning (2018)	
Andrade empirical exponent	α	0.3	...	Jackson et al. (2002); Renaud & Henning (2018)	
Andrade empirical timescale	ζ	1.0	...	Efroimsky (2012); Renaud & Henning (2018)	
Additional parameters ^c					
Reference grain size	d_{ref}	3.1×10^{-6}	m	...	
Grain size exponent	m	1.31	
Reference temperature	T_{ref}	1173	K	Jackson et al. (2010); Padovan et al. (2014)	
Reference pressure	P_{ref}	0.2	GPa	...	
Activation energy	E_{act}	303×10^3	J mol ⁻¹	...	
Activation volume	V_{act}	10^{-5}	m ³ mol ⁻¹	...	
Gas constant	R_g	8.314	J K ⁻¹ mol ⁻¹	Tiesinga et al. (2020)	

Notes.

^a In ALMA, we replace s with $i\omega$ (see the text), where $\omega = 88$ days.

^b In Renaud & Henning (2018), compliance J (the inverse of shear rigidity μ) is used. The defect is defined such that relaxed compliance $J_R = J_U + \delta J$.

^c Used to relate viscosity to pressure and temperature via the Arrhenius relation, see Equation (14).

We compute the multilayer solid tidal response of Mercury in order to obtain values for k_2 for a given internal structure with the ALMA software (Spada 2008). This software computes the potential and displacement Love numbers for a spherically symmetric, viscoelastic planet that is considered incompressible. Because of Mercury’s relatively small size, it can be treated as such. We made several changes to the software for it to be applicable to our case, and to include more rheological laws. We replace ALMA’s Laplace variable s with its Fourier counterpart $i\omega$, where ω is the tidal forcing frequency (which we assume is equal to Mercury’s orbital motion) and $i^2 = -1$. In this context, the Laplace and Fourier approaches are formally identical (Peltier 1974), each having certain advantages depending on the case (e.g., Jara-Orue 2016). We add the Andrade (Andrade 1910) and Sundberg–Cooper (Sundberg & Cooper 2010) rheological laws for use in ALMA. The Andrade model has been used extensively in tidal studies of Mercury, and increasingly for many other bodies as well. We add the recently developed Sundberg–Cooper rheology because it shows excellent correspondence with laboratory experiments on materials relevant to Mercury’s mantle in particular (Renaud & Henning 2018). We use the formulations of these rheological laws as given in Renaud & Henning (2018) to express them in terms of the complex shear modulus $\bar{\mu}$, as used in ALMA Spada (2008), Table 7. Table 3 shows the explicit formulas as used in ALMA, along with a list of the additional parameters that we use in our viscoelastic tidal deformation modeling, together with their values.

We pass the parameters of our self-consistent interior structure models to ALMA to compute the Love number k_2 .

The ALMA software assumes a uniform core, so it is either solid or liquid, and we assume, for the tidal response, an entirely liquid core. We use the average core density from our models as the density of this uniform core. This does not affect our results because the contribution of the solid inner core (and the density stratification within the core) to the Love number is deemed negligible (Padovan et al. 2014). Steinbrügge et al. (2018a) also show only a minor influence on the Love number, and indicate that a linear combination, or the ratio, of the vertical surface displacement Love number h_2 and the potential Love number k_2 cancel the ambiguity to some extent. We do not use h_2 as a constraint in this analysis, and we thus do not take the solid inner core into account. The liquid core is assigned zero rigidity.

For the mantle, we make a detailed model because the Love number is strongly determined by the mantle’s structure and properties. We assume a conducting mantle, following earlier works (Padovan et al. 2014; Steinbrügge et al. 2018a, 2021). Padovan et al. (2014) remarked that a convecting mantle can be mimicked to some extent by varying the temperature at the CMB in a conducting model. Higher CMB temperatures would have a similar effect as the more deformable convecting mantle, where the temperature would be relatively constant, and approximately equal to the CMB temperature. In our modeling, higher constant temperatures in the mantle will likely affect the resulting k_2 value by increasing it, but this can be counteracted by other parameters in our MCMC analysis. We will thus use a wide range of CMB temperatures in our analysis. We will discuss a case that mimics a convecting mantle in Section 4.2.

For the conducting mantle temperature profile, we solve the radial heat conduction equation for a sphere (e.g., Turcotte & Schubert 2002):

$$k \frac{1}{r^2} \frac{d}{dr} \left(r^2 \frac{dT}{dr} \right) + \rho H = 0, \quad (12)$$

where k is the thermal conductivity and H is the heat generation. We follow Padovan et al. (2014), where heat production in the crust H_c and mantle H_m are constant, with $H_m = H_c/2.5$. We use $H_c = 2.2 \times 10^{-11} \text{ W kg}^{-1}$, which is the heat production at the surface as derived from MESSENGER measurements (Peplowski et al. 2011). As boundary conditions, we set the temperature at the surface to be 440 K, and we use the value from our interior models for the temperature at the CMB. The thermal conductivity is set to $3.3 \text{ W m}^{-1} \text{ K}^{-1}$ (Michel et al. 2013; Padovan et al. 2014), for both the crust and mantle. With constant densities in the mantle and crust, and constant heat production, the conduction equation can be solved analytically, which results in a temperature profile $T_i(r)$ in a layer with constant density ρ_i and constant heat production H_i of

$$T_i(r) = -\frac{\rho_i H_i}{k} r^2 - \frac{C_1^i}{r} + C_2^i, \quad (13)$$

where C_1^i and C_2^i are integration constants. These constants are different for the crust and mantle profiles, and can be obtained from the boundary conditions—the surface temperature of 440 K and the CMB temperature—and from assuming a continuous temperature profile so that, at the crust–mantle boundary, the temperatures and their first derivative are equal for both profiles.

The viscosity η in the mantle is given through an Arrhenius law that takes into account temperature, pressure, and grain size (e.g., Jackson et al. 2004, 2010; Padovan et al. 2014):

$$\eta = \eta_{\text{ref}} \left(\frac{d}{d_{\text{ref}}} \right)^{-m} \exp \left[\left(\frac{E_{\text{act}}}{R_g} \right) \left(\frac{1}{T} - \frac{1}{T_{\text{ref}}} \right) \right] \times \exp \left[\left(\frac{V_{\text{act}}}{R_g} \right) \left(\frac{P}{T} - \frac{P_{\text{ref}}}{T_{\text{ref}}} \right) \right], \quad (14)$$

where d is the grain size (which is homogeneous throughout the mantle in our analysis), E_{act} is the activation energy, R_g is the gas constant, and V_{act} is the activation volume. The subscript “ref” indicates reference values. We use the values from Padovan et al. (2014), which are listed in Table 3. We also set the unrelaxed rigidities μ for the mantle and crust, and have them vary in our analysis. The crust itself has an infinite viscosity, as it is considered perfectly elastic. We tested this implementation against existing tidal codes in our group, such as the propagator matrix method used in Henning & Hurford (2014).

2.3. Markov Chain Monte Carlo Method for Determining Likely Interior Models

The previous two sections explained how we generate self-consistent models of Mercury’s interior, and how we can compute the moments of inertia, average density, and tidal response for each model. We now use this modeling together

Table 4
Parameters and Bounds Used in the MCMC Method

Parameter	Lower Bound	Upper Bound
Inner core radius	0	Outer core radius
Outer core radius	Inner core radius	Planet radius minus crustal thickness
Crustal thickness	0	150 km
Mantle density	Crustal density	3600 kg m^{-3}
Crustal density	2600 kg m^{-3}	Mantle density
Temperature at CMB	1600 K	2000 K
Weight fraction Si ^a	0%	20%
Unrelaxed crustal rigidity	50 GPa	60 GPa
Unrelaxed mantle rigidity	55 GPa	75 GPa
Grain size	1 mm	3 cm
Mantle reference viscosity	10^{20} Pa s	$2 \times 10^{23} \text{ Pa s}$

Note.

^a Weight fractions for the inner and outer core are nominally the same, but can be separate. If separate, we enforce a smaller fraction for the inner core.

with an MCMC method to determine the probability density functions of the parameters of these interior structure models that satisfy the geodetic measurements. We follow the exact same procedure as detailed in Genova et al. (2019). We use the Metropolis–Hastings scheme (Metropolis et al. 1953; Hastings 1970) to explore the parameter space.

We list the parameters that we vary, together with the bounds that we impose, in Table 4. We have 11 parameters, but only three to four target properties (with the bounds set on the parameters as additional constraints). We thus use MCMC to explore the parameter space, and do not expect to find all parameters equally well-determined. As in Genova et al. (2019), we start off with a set of parameter values that we randomly perturb, and then we compute a number of models (in our case, 500,000). We start this same procedure several times, with each being called a chain. We run 20 chains, after which we randomly mix the results from these chains. We skip the first 20,000 models (the burn-in period) because the randomized start models may be so perturbed as to not even be from the target distribution. We choose one model each time from the 20 chains, so we end up with $\sim 480,000$ models in total, randomly taken from each chain of 480,000 remaining models. In total, for each run, 10,000,000 self-consistent models are thus created and evaluated. We do this in order to ensure a mapping of the parameter space as complete as possible, in case one or more chains get stuck on a local minimum of the target metrics.

For each model in each chain, we compute the deviation of three to four target properties, weighted by their errors, to compute a probability that is used in the MCMC method either to accept or reject a model when it is tested against a uniform distribution, according to the Metropolis–Hastings scheme. Assuming a Gaussian distribution for each target, we compute the probability function $p(j)$ for the j -th model as

$$p(j) = \exp \left(\frac{1}{2} \mathbf{dx}^T \mathbf{C}^{-1} \mathbf{dx} \right), \quad (15)$$

with \mathbf{dx} being the 3×1 (or 4×1) vector of differences of the model and target property, and \mathbf{C} being the target property covariance matrix, which here we assume to be diagonal, with the diagonal elements being the square of the target property errors (see also Section 3.1). If the probability ratio $p(j)/p$

$(j - 1)$ is larger than a draw from a uniform distribution, then the model is accepted.

As target properties, we include the polar and crust–mantle moments of inertia, the global average density, and, optionally, a fourth measurement constraint through the tidal response characterized by k_2 . The results below are labeled as to whether they include k_2 as a fourth measurement constraint, or instead derive it freely as a prediction. We use the different measurement values from Table 1 in order to explore the influence of the different moment of inertia measurements. For all of the studies listed there, we use a 0.2% error on the planet’s average density. In this way, we compute a large quantity of models, with the underlying goal of mapping out the parameter space that satisfies the measurements and their errors. Taking the error on the measurements into account is an important aspect of the MCMC method, because it allows for the determination of the probability distributions of the interior model parameters, which focusing on models consistent with only the central values does not. In addition to the parameters listed in Table 4, we also collect information on Mercury’s interior for each model, such as the isothermal inner core temperature T_{ICB} , the core pressure at $r = 0$, P_{center} , and the displacement Love numbers h_2 and l_2 .

3. Results

We focus here on two sets of measurements from Table 1: those by Genova et al. (2019), as an example of the lower polar moment of inertia, and those by Mazarico et al. (2014). The latter’s normalized polar moment of inertia is 0.349, which is close to the value from more recent studies, such as those by Stark et al. (2015) and Bertone et al. (2021), that also find an obliquity larger than that of Genova et al. (2019). We use the results of Mazarico et al. (2014) here because they also co-estimated k_2 . Other more recent results have similar polar moment of inertia values, but did not estimate k_2 because they used measurements, such as radar or laser altimetry, tied to the surface, and hence it would not be readily clear which k_2 estimate from the analyses based on tracking data to use. We analyzed other measurements (by Hauck et al. 2013, Konopliv et al. 2020, and Bertone et al. 2021), and throughout this section we will mention results from those analyses to further illustrate certain points. All analyses were performed using the MCMC method, as described in Section 2.3.

Our results of course depend on the set of parameters that we varied in our MCMC analysis (see Table 4). While we focus on a subset of parameters in this section, in the figure set we show the a posteriori distributions for the measurements that we used (Figures A3.1–A3.4), for the set of parameters that we varied (Figures A3.5–A3.15), and for the parameters, such as core densities, that are derived (Figures A3.16–A3.18).

In this section, we will first focus on how well the different measurement sets are mapped, by using k_2 both as a measurement and by predicting it. We then illustrate how the estimate of the CMB radius is affected by the different measurement sets. In addition, we revisit the existence of the solid inner core. We also show results for crust and mantle properties, and for the composition of the core, expressed as weight percentages of Si. Finally, we show additional parameters derived from our solutions. All of the results in this section are performed with the Andrade rheology, and we leave a discussion of the influence of rheology for Section 4.4.

3.1. Distributions of the Measured Quantities

The MCMC analysis explores the parameter space, given the measurements and their errors. Here, we inspect how well our MCMC analysis maps out the measurements of the different studies. In Figure 1, we show the polar moment versus crust–mantle polar moment, and polar moment versus k_2 , for the models from our MCMC analysis. Models are binned for the heat map from the point cloud of all of the models. Each point in the cloud represents one model that was accepted in our MCMC run. Each point in that cloud is thus consistent with the measurements, within their given errors. Each model itself is, of course, defined by the parameter values as described in Table 4. The target ellipse is constructed as an ellipse centered on the central value, with axes scaled by the quoted error. This constitutes the target that the models should match. We also include the ellipse of the ensemble average, constructed from the average and the standard deviation around this average. If the measurements are consistent, the target and ensemble ellipses should overlap for all measurements. For all of the cases (irrespective of the measurement set used), the planet’s average density is always matched.

Figure 1 shows that when using the measurements of Genova et al. (2019), we can map the measurements of $C/(MR^2)$, C_m/C , and k_2 very well. Even when we do not include k_2 as a measurement, its prediction (Figure 1(G)) is still very close to the actual measured value. This is different when we use the measurements from Mazarico et al. (2014). When we include k_2 as a measurement, the polar moment $C/(MR^2)$ cannot be mapped well, and a smaller moment of inertia is preferred. However, k_2 itself (Figure 1(F); vertical axis) is mapped well, because the ensemble k_2 range matches the target k_2 range; the offset in the target and ensemble ellipses comes solely from not matching the polar moment. This indicates that this solution is clearly dominated by the k_2 measurement, because of its tighter error. Moreover, the k_2 and $C/(MR^2)$ measurements are incompatible because the ensemble and target ellipses do not overlap (Figures 1(B) and (F)). When we do not include k_2 as a measurement, we can map the moments of inertia (Figure 1(D)), as the ellipse for the ensemble average is within that of the target. The predicted k_2 for these models has an average value of 0.63 (Figure 1(H)) and is in general higher than the Genova et al. (2019) value of 0.569, which was already higher than the 0.451 value of Mazarico et al. (2014), although the results show a wide range of likely k_2 values. We reiterate that the k_2 estimate of Genova et al. (2019) is based on the entire MESSENGER data set, including the low-altitude data, which were not included in the estimate from Mazarico et al. (2014).

All of the results show clear concentrations of models around the central values, as indicated by the warmer colors in Figure 1, except for the case where we used the results from Mazarico et al. (2014) for the polar moment versus the crust–mantle polar moment when we predict k_2 . This is due to a larger spread in the polar moments, possibly due to the larger error.

We also note that when we predict k_2 , there is a correlation between $C/(MR^2)$ and k_2 , as indicated from the slope of the point clouds in Figures 1(G) and (H). We could readily include covariance information in our analysis (by using a full covariance matrix C in Equation (15)), but for the purposes of simplicity and comparison with earlier works we opted not to do this. However, Figure 1(G) shows that we still

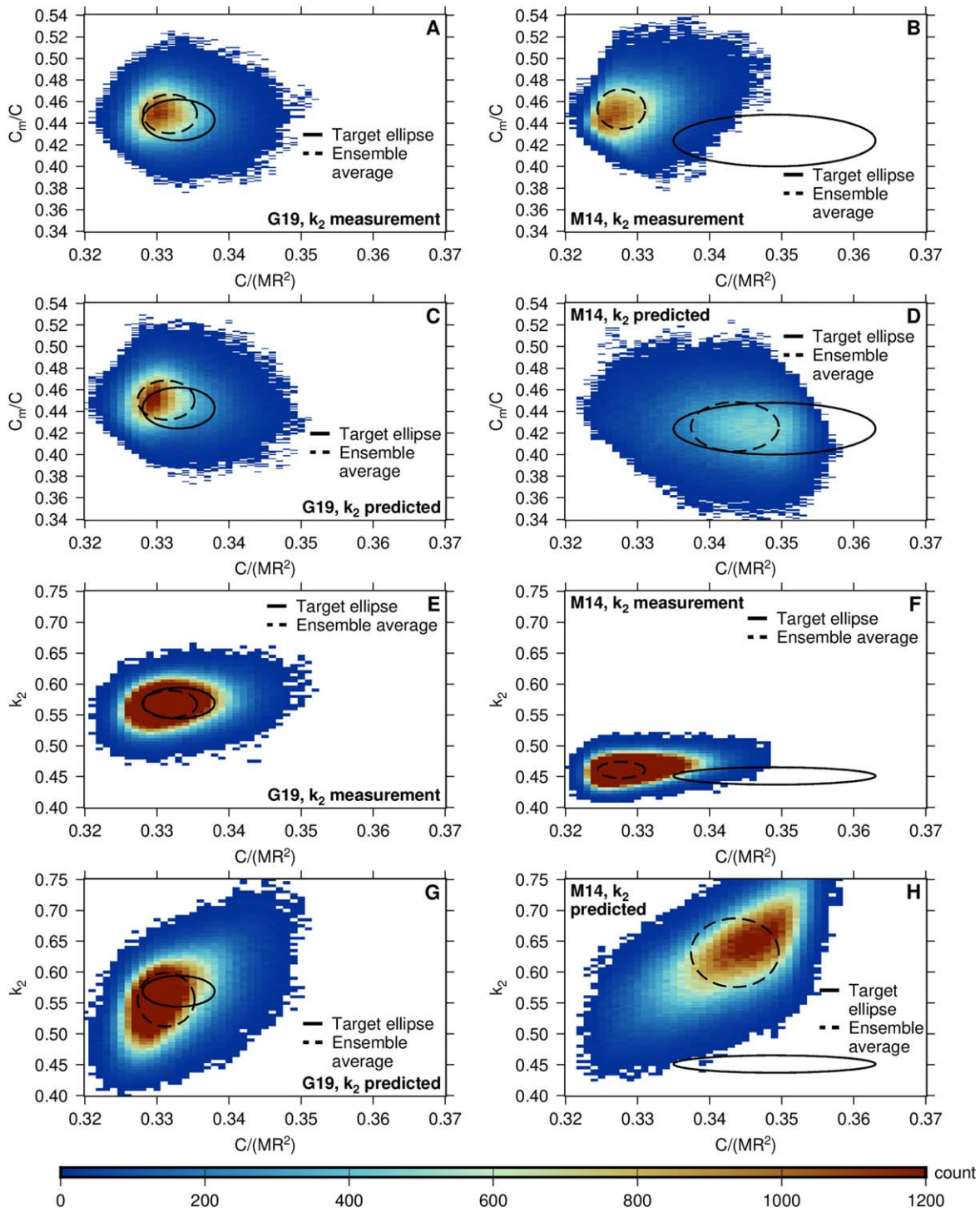


Figure 1. Results from the MCMC analysis, where we plot the entire polar moment vs. the crust–mantle polar moment (A–D) or the entire polar moment vs. k_2 (E–H). We indicate the concentrations of the models with colors. We include ellipses for the measurements (the “target”) as well as for the ensemble average. We use the measurements from Genova et al. (2019), indicated as G19, or Mazarico et al. (2014), indicated as M14. We include k_2 in the analysis as a measurement (indicated with “ k_2 measurement”), or do not include it as a measurement but instead predict it (“ k_2 predicted”).

map the measurements well without this additional covariance information.

We also used the measurements of Hauck et al. (2013) and Bertone et al. (2021) in our analysis. We show similar heat maps as shown in Figure 1 in the Appendix in Figure A1. Both of these studies had polar moment values closer to that of Mazarico et al. (2014). Figure A1 shows that we can readily match the observations. Neither of the studies estimated k_2 , and

our predictions for k_2 (Figures A1(C) and (D)) show values higher than 0.569 in general, the same as we show for the results using Mazarico et al. (2014) in Figure 1(H).

Finally, we also performed an analysis with the measurements of Konopliv et al. (2020). We used two sets of measurements because of the discrepancy between their obliquity and pole coordinates. We show heat maps for these results in Figure A2. We can match the observations for both

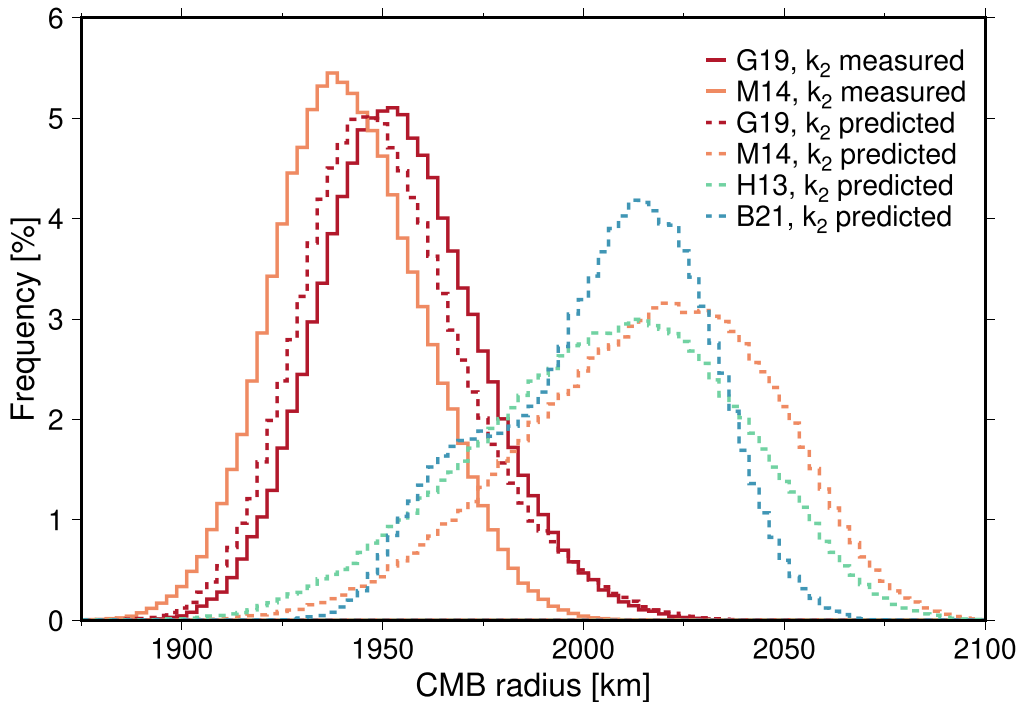


Figure 2. Results from the MCMC analysis for the liquid outer core radius (CMB radius), when using different measurements. We include cases where k_2 was used as a measurement (the solid lines), and cases where it was predicted (the dotted lines). We now also include measurements from Hauck et al. (2013; H13), and Bertone et al. (2021; B21), with k_2 predicted.

the lower (Figure A2(C)) and higher (Figure A2(D)) polar moment values when we do not include k_2 as a measurement. When we do include k_2 as a measurement in our MCMC analysis, we find a preference for lower polar moment values, even when the targeted polar moment of inertia has the higher value of 0.345 (see Figures A2(A), (B), (E), and (F)). This is because the quoted error on the polar moment is relatively large, and the MCMC analysis thus mostly fits the k_2 measurement. When we predict k_2 , we can match the higher polar moment (Figure A2(D)), but this results in a higher k_2 value than reported ($k_2 = 0.611$; see Figure A2(H)). This is consistent with our finding that using the result of Mazarico et al. (2014) without k_2 results in a predicted value of k_2 that is higher than the current estimate of 0.569. The k_2 value from Konopliv et al. (2020) is close to the k_2 value from Genova et al. (2019), and our analysis shows that it is more consistent with the lower polar moment value.

3.2. CMB Radius

Previous studies have already indicated that the parameter that is best determined from measurements of moments of inertia is the CMB radius (e.g., Hauck et al. 2013; Knibbe & van Westrenen 2015; Margot et al. 2018; Steinbrügge et al. 2021). We show the a posteriori distributions for the CMB radius for various MCMC analyses in Figure 2. Two distinct peaks are visible in the CMB radius distributions. The lower polar moment values result in smaller CMB radii, and the higher polar moment values result in larger CMB radii. These results are entirely consistent with earlier analysis by Hauck et al. (2013) and Knibbe & van Westrenen (2015), when using the higher polar moment value from Mazarico et al. (2014), and with Genova et al. (2019) when using the lower polar moment value (see also Table 1). For the result using the measurements from Mazarico et al. (2014), we also find a smaller CMB radius

when we include k_2 as a measurement, despite their higher polar moment value. As we showed in Figure 1(B), this particular case also results in a preference for a lower polar moment because of the tight constraint on k_2 : the MCMC analysis is entirely dominated by satisfying the k_2 measurement over the polar moment one. When we use the measurements of Genova et al. (2019), we find a CMB radius of 1955 ± 20 km. When we use the higher polar moment value of Mazarico et al. (2014), we find a CMB radius of 2015 ± 31 km.

Steinbrügge et al. (2021) indicated that the smaller core size is not consistent with recent estimates from magnetic induction. Indeed, Wardinski et al. (2019) found a value of 2060 ± 22 km. However, other magnetic studies found much larger error bars on their core radii. Johnson et al. (2016) found values between 1900 and 2060 km, and a more recent study by Katsura et al. (2021) found a value of 2011 ± 180 km. Both these results cover the CMB radius from both polar moment values. We thus consider that the results from magnetic studies to date do not strongly constrain the allowed range of CMB radii.

In general, k_2 is sensitive to the CMB radius because it defines the thickness of the mantle. The thickness, and stiffness, of the mantle (and crust) then determine the extent of the tidal response. Hence, a lower k_2 value, as reported by Mazarico et al. (2014; and confirmed by Verma & Margot 2016 using the same data), is indeed expected to result in a lower CMB radius value. Conversely, higher polar moment of inertia values are expected to result in larger CMB radius values. Our modeling results show both of these behaviors. This is also pointed out in Steinbrügge et al. (2021), when they raise the issue and the possible incompatibility of the lower polar moment of Genova et al. (2019) and the higher k_2 value of 0.569. Importantly, our results indicate that these measurements are actually compatible. Our results are also still consistent with this dependence of k_2 on the CMB radius, as

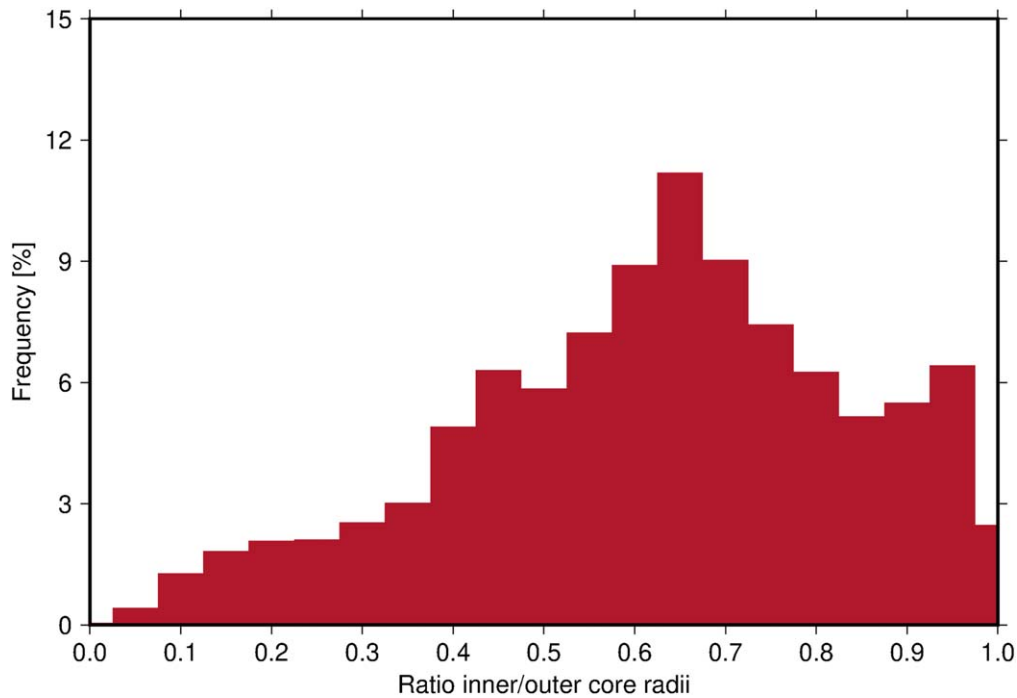


Figure 3. The ratio of the radii of the inner core and outer core when using the measurements of Genova et al. (2019), now including k_2 as a measurement.

shown by the predicted k_2 values in Figures 1(G) and (H), and by the CMB radii from Figure 2. For the larger moment of inertia values, we find larger CMB radii, and generally higher k_2 values. Our results show that the discrepancy may not be in the moment of inertia and k_2 results of Genova et al. (2019), but rather in the incompatibility of the higher moment of inertia values from other studies and the earlier, lower value for k_2 , which was not based on the entire MESSENGER data set. Other parameters, such as viscosity, temperature, and grain size, also have an effect on the resulting k_2 (e.g., Padovan et al. 2014; Steinbrügge et al. 2018a, 2021). We discuss this further in Section 4.

3.3. Existence of the Solid Inner Core Revisited

Our interior models include a solid inner core of variable size, and because our viscoelastic tidal deformation modeling does not take into account a solid inner core, as explained above in Section 2.2, we do not expect the results to change from those reported in Genova et al. (2019), although of course correlations with other parameters now determined from the tidal response could have an effect. In Figure 3, we show the ratio between the solid inner core and liquid outer core radii. This result is similar to that of Genova et al. (2019) for a structure with an FeSi core, and this indeed shows that our modeling that now includes k_2 still indicates evidence for the existence of a solid inner core.

In addition, we investigated the average densities of the cores of our solutions. In Figure 4, we show the average density of the solid and liquid parts of the core for each MCMC model, plotted against the resulting ratio between inner and outer core radii. We obtain the average core density through integration over the layers once the model has been constructed. Figure 4 shows a clear difference between the densities of the solid and liquid parts, except for the large inner cores, where the inner core densities are close to liquid core values. They are never smaller, however, because we enforce this. A low core density

is due to a high weight fraction of Si (we discuss the Si weight fractions in more detail in Section 3.5).

For inner cores larger than ~ 0.6 times the radius of the CMB, the densities of the inner core are in the range of liquid values. We note, however, that the inner core local density is derived with a solid EOS, and thus is consistent with a solid value at the given pressure and temperature. We discuss the effects of local pressure and temperature on the state of the core in Section 4.3. On the other hand, the density of the liquid core becomes lower as well. This is because we only accept models that have a density contrast at the boundary of the inner and outer cores.

The lower polar moment makes it more likely that a solid inner core is present, as it indicates denser materials toward the center. We find again a clear indication of a solid inner core, as shown in Figure 3.

3.4. Crust and Mantle Properties

Several of our estimated parameters (recall that we show their distributions in the figure set in Figures A3.5–A3.15) show flat distributions, indicating that our results are not sensitive to their values in our modeling. This includes the crustal density and crustal thickness, as well as the temperature at the CMB, the grain size, and the rigidities. For the mantle (and crust) rigidities, we allow a range of values, since we opt to remain agnostic about the mineralogy of the mantle. The flat distributions for these parameters indicate our results are not particularly sensitive to them.

Although it appears that our results favor lower crustal densities (Figure A3.8) and higher crustal thicknesses (Figure A3.9), it should be kept in mind that the crustal density especially trades with the mantle density. We enforce a higher density for the mantle compared to the crust, so the crustal density distribution shows fewer models as the crustal density approaches the mantle density. For the crustal thickness, the

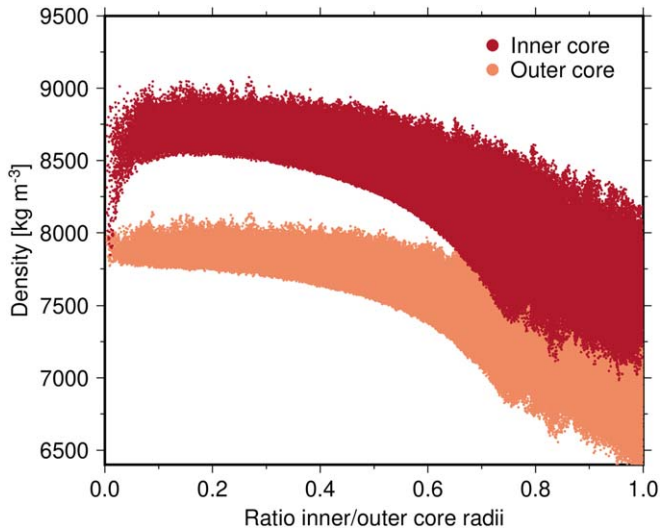


Figure 4. The ratio of the radii of the inner core and outer core vs. the liquid or solid core density. These results are from the MCMC analysis using the measurements of Genova et al. (2019), including k_2 .

distribution is skewed toward thick crusts, but we find no dependencies with other parameters.

Our mantle densities are lower than those from the earlier analysis by Hauck et al. (2013; see Figure A3.7). We find an average value of $3089 \pm 135 \text{ kg m}^{-3}$ from our distribution. The earlier analysis by Genova et al. (2019) found an average value for the mantle density of $3145 \pm 154 \text{ kg m}^{-3}$. These values are consistent at the level of one standard deviation, but our value is on the lower end. While most of our results are consistent or very similar to those presented in Genova et al. (2019), we do find some differences (in the CMB radius, weight fractions of Si in the core, and mantle density), which are due to our strict enforcing of density contrasts at the ICB.

Low mantle density values are also discussed by Steinbrügge et al. (2021), who state that they could risk an inconsistency between the expected composition of the mantle and the resulting density from the interior modeling. We indeed find similar results to Steinbrügge et al. (2021) for the mantle, with lower values for the lower polar moments. The spread that we find would still allow many models with higher values, however. When we use the higher polar moment values, the mantle density increases to $3237 \pm 186 \text{ kg m}^{-3}$ (when using the values from Bertone et al. 2021), or to $3317 \pm 181 \text{ kg m}^{-3}$ (when using the polar moment from Mazarico et al. 2014). We also find higher mantle densities for larger weight fractions of Si in the core (see Figure A3.19), as larger amounts of Si bring down the average core density.

3.5. Composition of the Core

Core composition is determined in our models by the weight fraction of Si. This is an important quantity because it can connect Mercury formation conditions and models to the measured surface abundance of Si (e.g., Chabot et al. 2014; Boujibar et al. 2021). In Figure 5, we show the a posteriori distributions for the weight fraction of Si in the core for various MCMC analyses. When we use the measurements of Genova et al. (2019), we find generally lower weight fractions in the core. The mean and median are 5.6% and 5.2%, respectively, with a peak showing in Figure 5 at around 4%. We also note that there is a relationship between the weight fraction of Si in

the core and the CMB temperature, just like there was between the weight fraction of Si in the core and the mantle density, as discussed in Section 3.4. We show this in Figure A3.20, and find that lower weight fractions generally mean higher CMB temperatures.

In our analysis, we assumed the weight fraction of Si to be the same in the solid and liquid core. However, as remarked earlier, because of the noted compositional contrasts between the solid and liquid layers (e.g., Fischer et al. 2014), we also include an analysis where we varied these weight fractions separately, with the only constraint being that the weight fraction of the inner core is smaller than that of the outer core. This analysis thus had an extra estimated parameter, as two weight fractions are now included. We include that result in Figure 5, and we note that this shifts the distribution peaks: the inner core has a lower weight fraction, whereas a higher weight fraction for the liquid core is allowed. From the histogram, it appears that the differences can be substantial, which is likely not in accordance with the experimental data, as the difference may amount to only several percent (Fischer et al. 2014). However, a heat map of the inner core weight fraction versus the outer core weight fraction (Figure A4(A)) shows that most solutions have a limited range in weight fractions, thus also limiting the difference between the two. If we further enforce a limit on the difference, the results are closer to those assuming the same weight fractions, and large Si weight fractions in the liquid outer core are generally not found (see Figure A4(B), where a maximum difference of 3% was used). We also note that when we use the higher polar moment of inertia in our analysis, the weight fraction for Si tends to come out higher ($\sim 15\%$; see Figure 5), consistent with the results from Hauck et al. (2013).

3.6. Results for Derived Interior Quantities

For each MCMC model, we also compute a set of additional values that characterize the interior. In Figure 6, we show a posteriori distributions for the displacement Love numbers h_2 and l_2 , and for the inner core temperature and pressure. A first data-based estimate for the radial displacement Love number h_2 was recently published by Bertone et al. (2021). Their result for h_2 is 1.55 ± 0.65 , and was derived using altimetric crossovers using MLA data. Due to the sparsity of crossovers from an elliptical orbit, this parameter is difficult to estimate. Their quoted error is based on a careful analysis of various effects, such as the variations in the constraint factor used, the start values used in their modeling, and the use of subsets of data. They then derived their error by taking into account the range of h_2 estimates from all of these various solutions, and it thus reflects a much more comprehensive analysis of the expected error than a straightforward formal error obtained from an inversion. Their value is higher than what our modeling predicts, although our value of 1.02 ± 0.04 is within their one-sigma bound. Future analysis using laser altimetry from the BepiColombo mission to Mercury may provide improved h_2 measurements (Steinbrügge et al. 2018b; Thor et al. 2020; Genova et al. 2021; Thomas et al. 2021), against which our predicted value can be tested. Alternatively, an estimate of h_2 can then serve as an additional measurement to better constrain the properties of Mercury's inner core (Steinbrügge et al. 2018a). The horizontal displacement Love number l_2 can likely only be measured from a lander (e.g., Ernst et al. 2021), but we include it here for completeness.

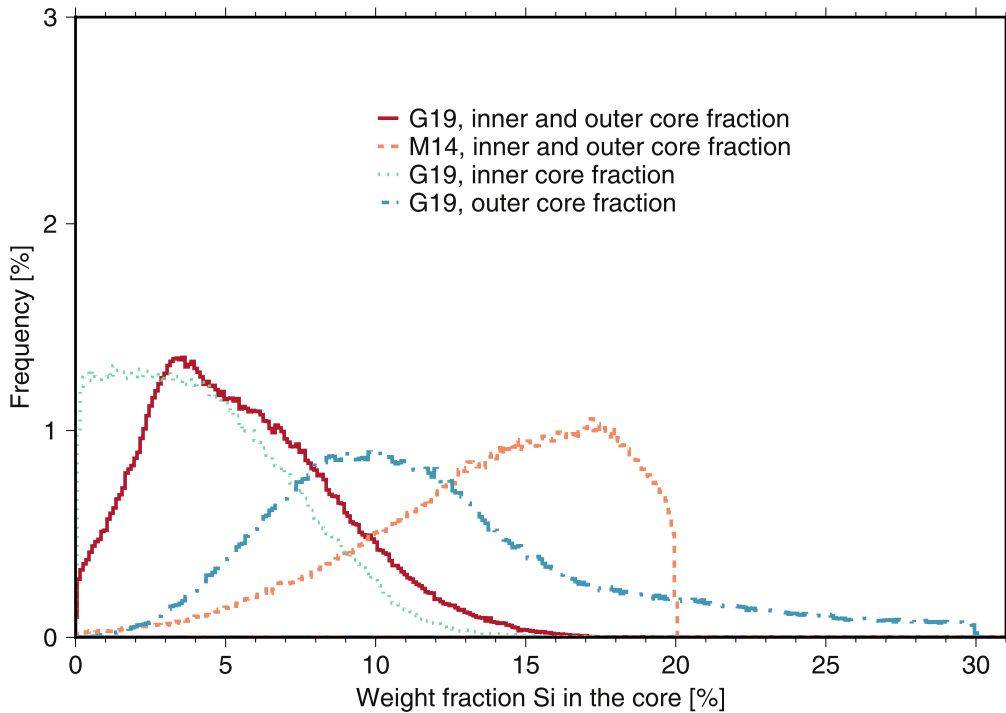


Figure 5. Weight fractions of Si in the core for the results from the MCMC analysis. We used the measurements from Genova et al. (2019; G19), where we either set the weight fractions of the inner core and outer core to be the same (labeled “inner and outer core fraction”), or separate (indicated by “inner” and “outer”). We also used the measurements from Mazarico et al. (2014; M14), where the weight fractions were set to be the same. The solid lines indicate where we included k_2 as a measurement (the G19 cases), and the dotted line indicates where we did not include k_2 as a measurement (the M14 case).

The inner core is assumed to be isothermal, so we obtain the inner core temperature for our models as the temperature of the liquid core at the ICB, as explained in Section 2.1. Together with the pressure, these variables can inform us of the core conditions important for studies of the formation, crystallization, and dynamo action of the core (e.g., Chabot et al. 2014; Dumberry & Rivoldini 2015), and hence we include their resulting values here as histograms (while we will show pressure versus temperature for the inner core in Figure 10). The core pressures from our models are consistent with those reported by Hauck et al. (2013), with a higher average value in our case because of the inclusion of the inner core, and higher densities toward the center as a result of the lower polar moment. Our core temperatures are consistent with those that have been discussed in earlier studies (e.g., Malavergne et al. 2010).

4. Discussion

Our MCMC analysis indicates that we can correctly map the observations of Genova et al. (2019), and that in principle there appears to be no incompatibility between the lower polar moment value of 0.333 and the higher k_2 values in the 0.53–0.57 range. Indeed, our results indicate that the higher polar moment value of around 0.346 should result in an even higher k_2 value. These results of course depend on the set of parameters that we varied in our MCMC analysis, the results of which we showed in the previous section. Here, we discuss additional characteristics of our solutions. We investigate the viscosity at the CMB, considerations about a convecting mantle, and modeling aspects of the inner core. Finally, we discuss the influence of rheological laws on our results.

4.1. Viscosity at the CMB

In this study, the viscosity profile of the mantle (Equation (14)) has a big influence on the resulting k_2 value. We show this dependency in Figure A5(A) and note that k_2 changes rapidly in the viscosity range of roughly 10^{16} – 10^{20} Pa s. Steinbrügge et al. (2021) discussed such low viscosity values in detail, and indicated that, in order to match the higher k_2 values, the base of the mantle may have a very low viscosity, which could be interpreted, for example, as Mercury’s mantle having a basal layer of silicate partial melt. We thus also investigated the viscosity at the base of the mantle for our MCMC models. As Equation (14) indicates, this depends on the pressure at the CMB, the temperature at the CMB, and the grain size. The latter two are parameters in our analysis, and because we use constant densities for the crust and mantle the pressure can be readily computed analytically. In Figure 7, we show the viscosity at the CMB versus the outer core radius, the temperature at the CMB, the grain size, and k_2 .

We first note that, like Steinbrügge et al. (2021), we find a wide range of viscosity values in our models that are compatible with the geodetic measurements of Genova et al. (2019), including the lower range that they highlighted. Larger k_2 values require lower viscosities, and because of the temperature dependence, higher CMB temperatures also result in lower CMB viscosities. We only find a very weak dependence on the grain size, and our models do not seem to favor small or large grain sizes (see also Figure A3.12), contrary to Steinbrügge et al. (2021).

While our results include models with low CMB viscosities, we also find plenty of models with higher CMB viscosities (Figure 7(A)). The count of the number of models in bins, as shown in Figure 7, does indicate a concentration at values between 10^{14} – 10^{16} Pa s, but many models also have higher

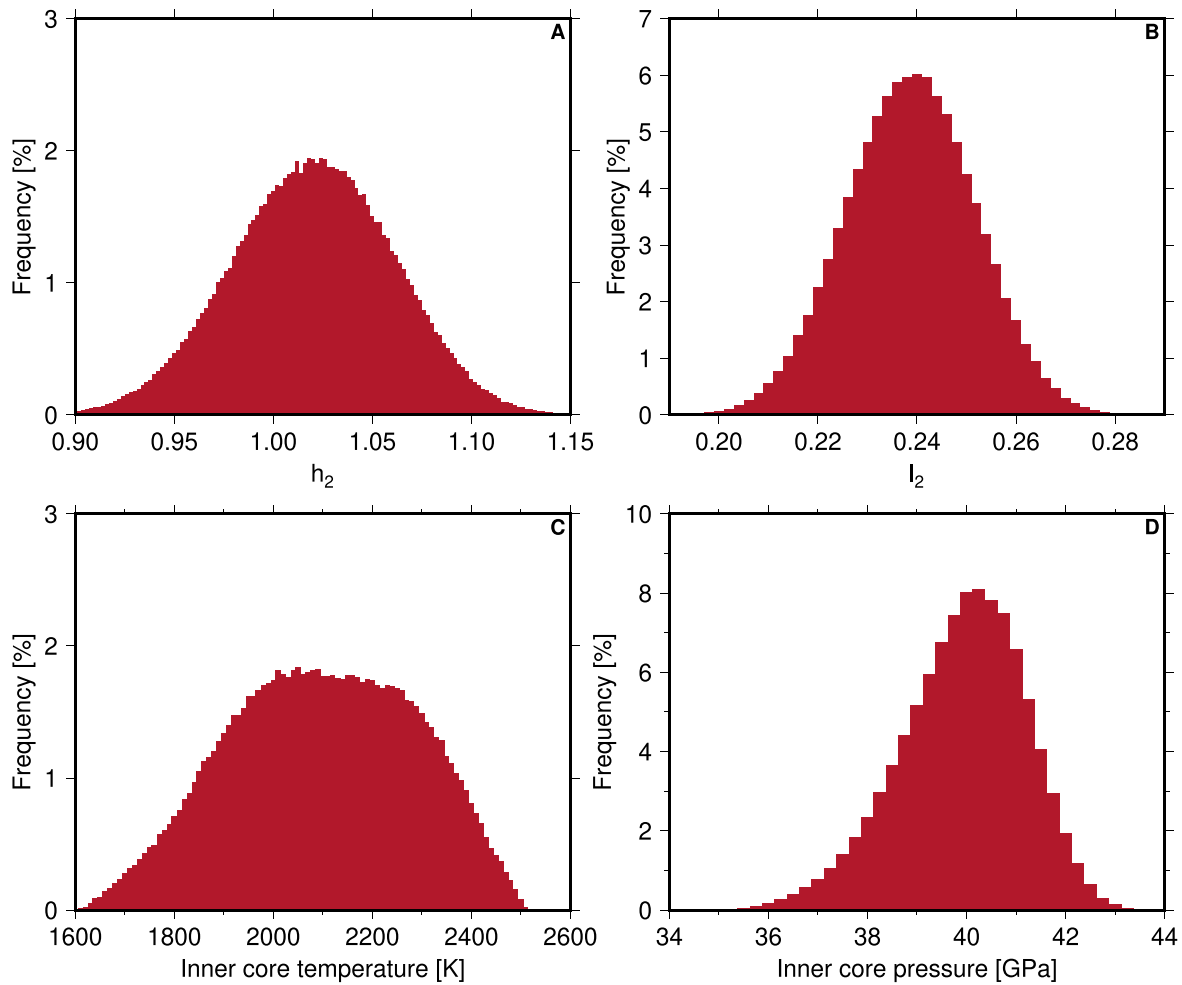


Figure 6. Predicted parameters from our MCMC analysis using the measurements from Genova et al. (2019), including k_2 . We present results for the vertical tidal displacement Love number h_2 (A), the horizontal displacement Love number l_2 (B), the inner core temperature (C), and the pressure at the center of the core (D).

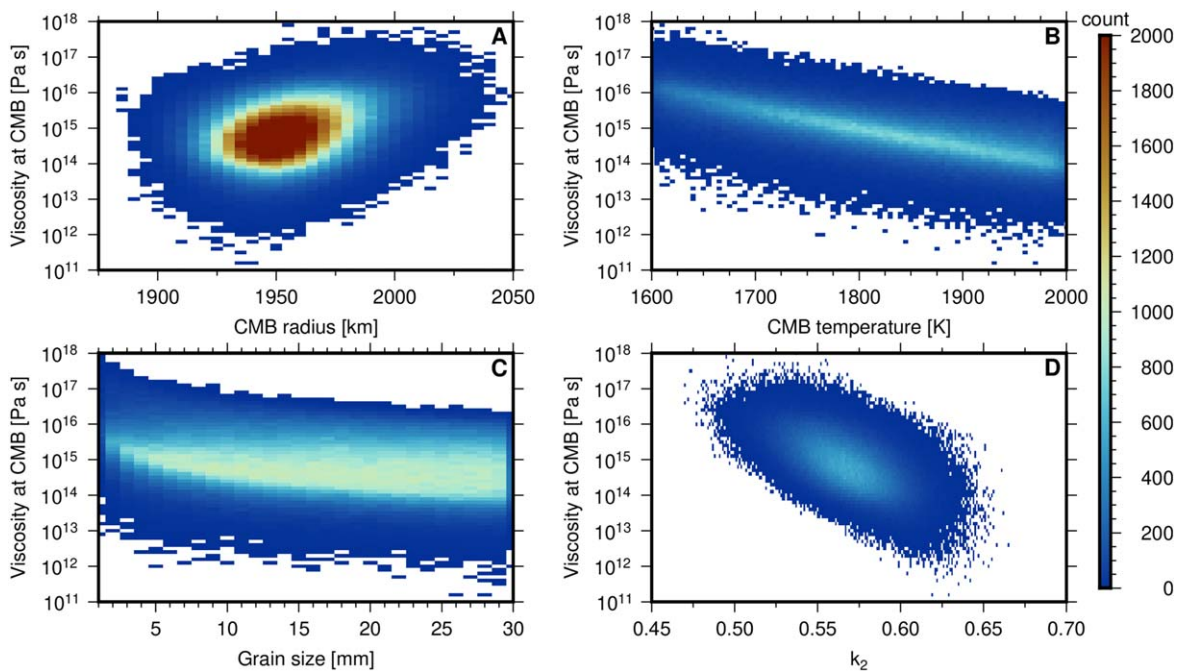


Figure 7. Viscosity at the CMB vs. the CMB radius (A), the CMB temperature (B), the grain size (C), and k_2 (D), from the results of our MCMC analysis using the measurements of Genova et al. (2019). We also indicate the number of models in bins (with a width of 0.1 in log space for viscosity, 5 km for CMB radius, 5 K for CMB temperature, 1 cm for grain size, and 0.001 for k_2) to highlight concentrations of models in the point cloud.

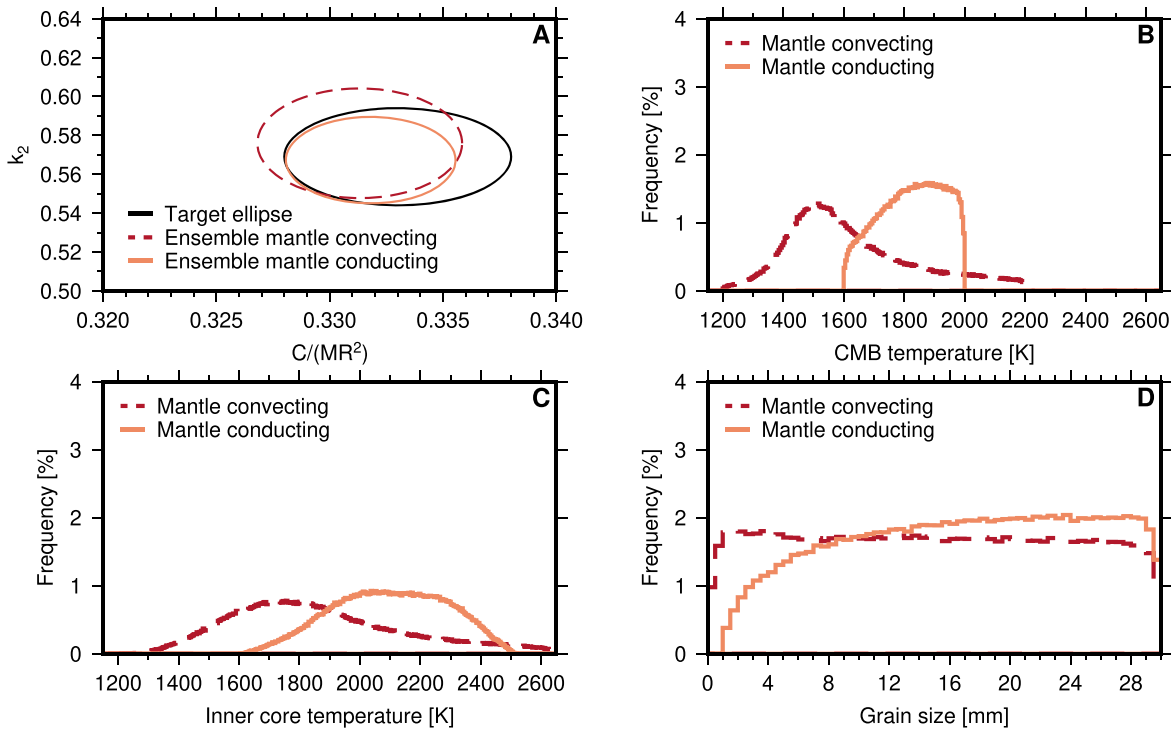


Figure 8. Ensemble and target ellipses for the results of our MCMC analysis using the measurements from Genova et al. (2019), where we now also include a convecting mantle, together with the results for a conducting mantle for comparison (A), and the resulting distributions for the CMB temperature (B), the inner core temperature (C), and the grain size (D).

values. There is of course also a straightforward relationship between CMB viscosity and the reference viscosity. Our analysis seems to prefer slightly higher reference viscosities (Figure A3.15), although one should also note their wide range, spanning several orders of magnitude. Lower reference viscosities (see Equation (14) for how this influences the viscosity profile) also result in larger values for k_2 .

We also do not find a preference for high CMB temperatures (Figure A3.10). While there seems to be a slight favoring of values on the higher end of our range, the distribution is very flat. The bounds for the CMB temperatures of 1600–2000 K (see Table 4) are based on earlier studies (Hauck et al. 2007, 2013), but this may be considered too limiting in the light of the results of Steinbrügge et al. (2021). Expanding the bounds to 1200–2400 K does not change the results, however. We find a wider distribution as a result (see Figure A6), which allows the higher values of Steinbrügge et al. (2021), but there is no preference for higher values as the peak in the distribution is still around 1800 K. We also do not find strong dependencies between the CMB temperature and other parameters, although lower CMB temperatures result in only slightly higher mantle densities and weight fractions of Si. Steinbrügge et al. (2021) found CMB temperatures of around 2100 K, and indicated that this can be problematic for a number of reasons, such as mantle melting, the presence of S, and volcanism. Our models do not show indications that such high temperatures are favored, or needed to fit the measurements, and our models thus avoid such issues.

4.2. Considering a Mantle with a Constant Temperature

While a conducting mantle is deemed most likely for Mercury (Tosi et al. 2013), a convecting mantle is not necessarily excluded (Michel et al. 2013; Tosi et al. 2013). As stated above, a

convecting mantle can be mimicked by selecting a range of CMB temperatures in our models. However, the temperature profile would still be conductive, whereas a convecting mantle’s temperature would be relatively constant.

While certainly not a complete model, we also performed an MCMC analysis with the measurements of Genova et al. (2019) by using a constant temperature in the mantle, which we set equal to the CMB temperature (we do not include a thermal boundary layer above the CMB). In this case, we extend the CMB temperature range to include values between 1200–2200 K, where we mostly expect to fall on the lower values, as a mantle at a constant high temperature will result in higher k_2 values than a conducting mantle with the same CMB temperature.

In Figure 8, we show the results from an MCMC analysis with a constant mantle temperature. We find that this model has more difficulty in mapping the combination of moment of inertia and k_2 , as the ensemble ellipse (Figure 8(A)) is offset toward lower moment of inertia values, whereas the ensemble ellipse for the conducting mantle case is entirely within the target ellipse (on the other hand, the ensemble ellipse for the convecting case covers more of the target ellipse). We do find lower CMB temperatures around 1500 K (Figure 8(B)), and also lower inner core temperatures, as a consequence (Figure 8(C)). We again find no clear dependence on the grain size (Figure 8(D)), for which we now also include values below 1 mm.

When we investigate the viscosity at the CMB (Figure 9, which is similar to Figure 7, but now for the convecting mantle case), we find higher values, with concentrations now at viscosities of 10^{17} – 10^{18} Pa s. The bulges with low CMB viscosity values in the scatter plot are related to the higher CMB temperatures in the model ensemble (Figure 9(B)). A convecting mantle, as modeled with a constant temperature,

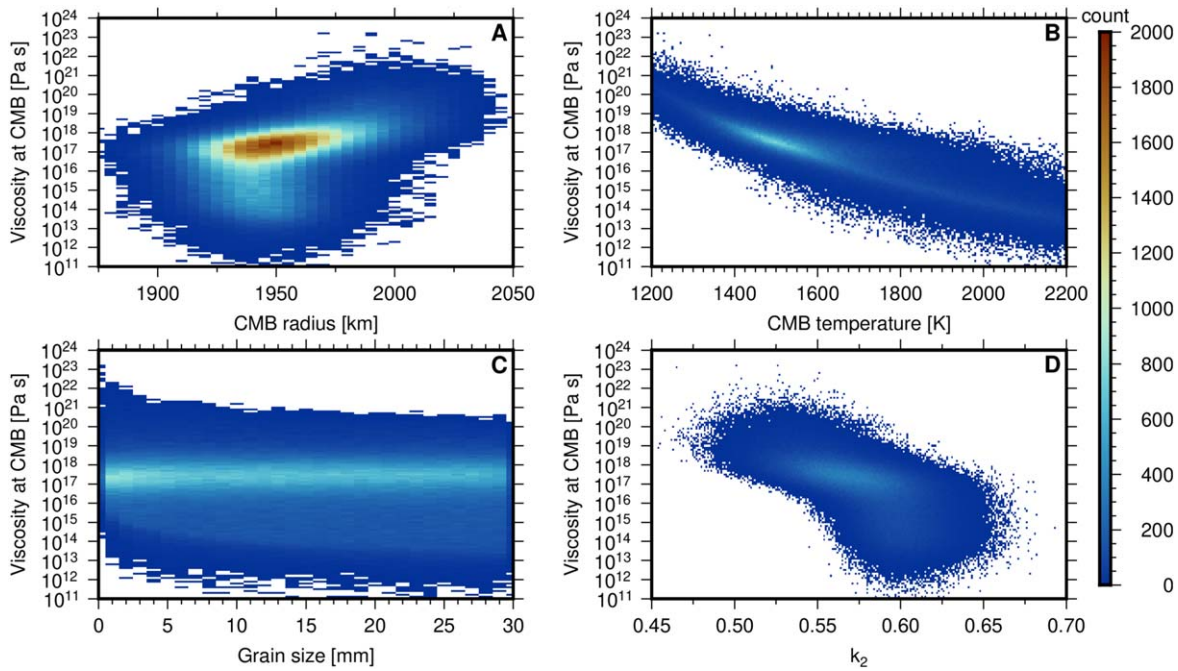


Figure 9. Viscosity at the CMB vs. CMB radius (A), CMB temperature (B), the grain size (C), and k_2 (D), from the results of our MCMC analysis using the measurements of Genova et al. (2019). For the results presented here, we modeled the mantle with one constant temperature when computing the tidal response, to mimic a convecting mantle. This temperature is equal to the CMB temperature, which is a parameter in the MCMC analysis. We extended the viscosity range, the CMB temperature range, and the grain size range, when compared to the results for the conducting mantle (Figure 7). We again indicate the number of models to highlight concentrations of models in the point cloud.

can thus alleviate the issues of low CMB viscosities, as found by Steinbrügge et al. (2021). On the other hand, it also results in a mapping of the target values that centers on lower polar moment of inertia values, slightly offset from the target of $C/(MR^2) = 0.333$ (see Figure 8(A)).

4.3. Considerations on Determining the Inner Core Size

As mentioned in Section 2.1, the choice to use the solid inner core as a parameter may result in thermodynamical inconsistencies. Using local pressure and temperature, and a melt curve, it can be determined whether the inner core indeed is solid at these local conditions for a given core size. We explored this for our set of models from the MCMC analysis using the results from Genova et al. (2019). We used melt curve information from Anzellini et al. (2013) for pure Fe, from Fischer et al. (2012) for FeSi at 16 wt% Si, and from Fischer et al. (2013) for FeSi at 9 wt% Si. For a given weight percentage of a model, we interpolate the melt curves to generate a new melt curve for a specific weight percentage. We then take the pressure at the inner core radius for the model under investigation, and the inner core temperature, and use the melt curve to test whether the material is solid. We do this after the MCMC run has been completed, not during.

We find that about 30,000 models out of our set of 480,000 are excluded in this way. This, however, does not affect the parameter distributions at all. In Figure 10, we show the pressure at the ICB versus the inner core temperature for our set of MCMC models. We also include the three melt curves that we used. Models where local conditions indicate that the core is still liquid, while it was assumed to be solid, are excluded. Figure 10 indicates the range of pressures and temperatures in the core. Models with lower weight percentages of Si in general have smaller inner cores, and hence the

pressure at the ICB is higher, or they have higher CMB temperatures (because the melt temperature for lower weight percentages of Si is higher).

Figure 10 indicates the presence of models with a low weight percentage of Si in the core and a low ICB temperature. Such models, especially those with temperatures far below the melt temperature of pure iron, as indicated by the melt curve from Anzellini et al. (2013), are deemed unrealistic, as they would likely need large amounts of other light elements, such as S, to bring down the temperature. As we do not model our core with an Fe–Si–S composition, it is thus possible that this could bias our results toward unrealistically cool end members. However, such models have high ICB pressures (as Figure 10 indicates), meaning they are models with small inner cores. Figure 3 (where the ratio between the inner and outer core radii is shown) and Figure A3.5 (where the inner core radius itself is shown) indicate that these models are not preferred in our set of solutions. We further illustrate this in Figure A7(A), where we turn Figure 10 into a heat map to indicate the number of models related to each pressure and temperature configuration. This shows that there are only a few models with high pressure, low temperature, and a low weight percentage of Si. This can also be seen in Figure A3.20, where there are only a few models with a low weight percentage and low CMB temperature, while most of the models show a trend with higher temperatures for low weight percentages.

If we exclude models that have weight percentages of Si less than 4% and that have a CMB temperature less than 1900 K, our parameter distribution does not change significantly, despite removing the substantial number of 82,771 models from our set (amounting to almost 20% of the number of remaining models). The average value for the mantle density increases from 3089 to 3103 kg m⁻³, and the polar moment of inertia appears to be mapped slightly better, with an average of

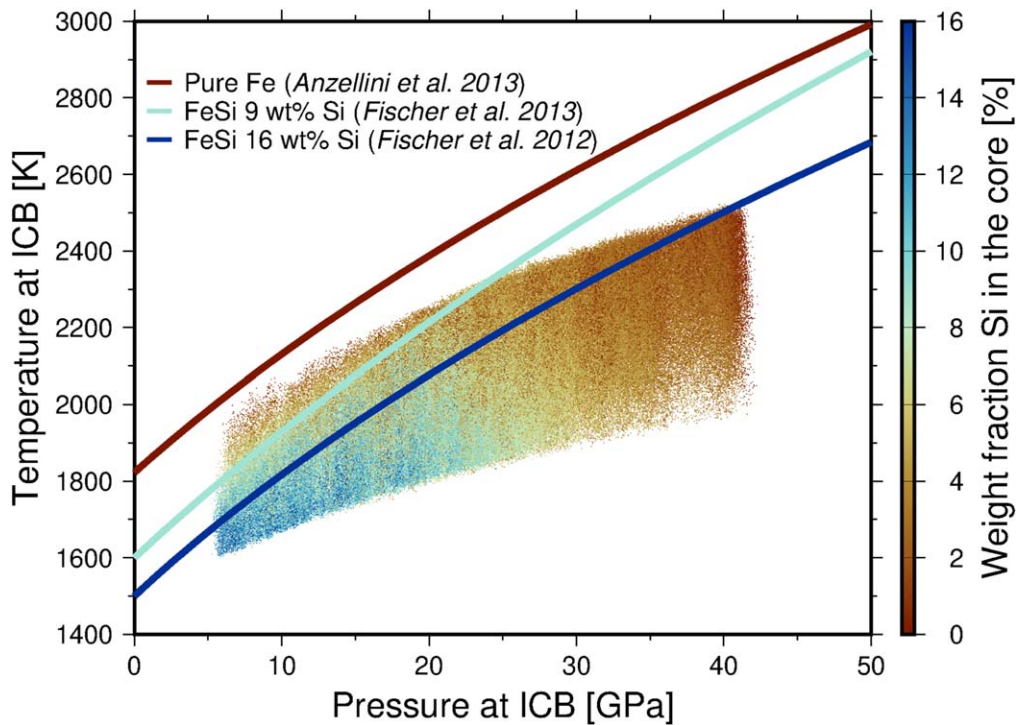


Figure 10. Pressure at the ICB vs. the temperature of the inner core, color-coded with the weight percentage of Si in the core for each MCMC model. Melt curves for pure Fe, FeSi at 9 wt% Si, and FeSi at 16 wt% Si are also shown. The results here exclude models where the core is assumed to be solid, but local conditions indicate that it is liquid.

0.3324 versus 0.3318 before. In Figure A7(B), we show a new pressure versus temperature plot, without these models. This now leaves hotter models at higher pressures, but we note again that such models with small cores are not preferred in our solution set.

It is also possible to use these melt curves to determine the inner core size from local conditions entirely. The results above exclude certain models because the conditions indicate that the core should be liquid and not solid, as we assume. It is also possible that, according to the melt curves, the transition from liquid to solid should occur at a larger radius (lower pressure), and that the solid core should thus be larger than assumed in our model. Determining the solid core size from local conditions and a melt curve would reduce the number of parameters, since now the inner core size would be determined from pressure and temperature, instead of being forced to occur at a certain radius. However, we chose not to pursue this for this study, as the temperature profiles in the core would become a strong driver for the size of the inner core. Several studies of the FeSi system indicate relatively large differences in melt temperatures for various weight percentages of Si (Asanuma et al. 2010; Fischer et al. 2012, 2013, 2014; Morard et al. 2014; Ozawa et al. 2016; Sakairi et al. 2017). With the current uncertainties on Mercury’s composition, the uncertain influence of impurities in Mercury’s core, and the uncertainties of the temperature profile in general, we find it more prudent to decouple the size of the inner core from the local conditions. The pressure–temperature range in Figure 10 may be conservative, but it shows the range of inner core pressures and temperatures in our set of models that match the observations of Genova et al. (2019), and can thus be of use in future analysis of core conditions (e.g., Tao & Fei 2021).

4.4. The Influence of Rheological Laws

Finally, we investigated the influence of rheology on our results. As stated in Section 2.2, we added the Sundberg–Cooper rheology to our tidal analysis. The rheology has an effect on the k_2 value through viscosity (see Figure A5(A)), and thus could potentially have an effect on the recovered parameters. We performed an additional MCMC analysis using the measurements of Genova et al. (2019) with this rheology instead of Andrade. Despite the possible differences in k_2 , we cannot distinguish between these rheological laws. For example, the mapped k_2 a posteriori distributions are nearly identical (Figure A5(B)). This indicates that the differences in tidal response expressed by the choice of rheology are absorbed in the parameter variations that we find. Because our results are not very sensitive to parameters that may have an influence through the rheology, such as the CMB temperature, we do not note a remarkable difference in the results. Improved or future measurements may result in better sensitivity with respect to the chosen rheology (e.g., Bagheri et al. 2019). The choice of rheology mostly remains based on performance compared to laboratory experiments. The Sundberg–Cooper rheology in effect adds the further mechanism of grain boundary sliding for grain-scale viscoelastic motion to a background Andrade model. However, this mechanism is only activated at certain temperature and forcing frequency regimes. Insensitivity to the Andrade versus the Sundberg–Cooper rheology choice may suggest that Mercury’s mantle is simply in a temperature/tidal forcing frequency domain reasonably well characterized by the Andrade-component grain-scale mechanisms. This, however, does not preclude the activation of grain boundary sliding in cooler regions of the layer structure, such as below the crust, where it may still be relevant for nonsynchronous spin tidal heat production.

5. Conclusions

Recent results of MESSENGER data analysis efforts for Mercury's orientation, as given by its obliquity, yield different values for its normalized polar moment of inertia $C/(MR^2)$, with either a low value of 0.333 (Genova et al. 2019) or a higher value of around 0.346 (Margot et al. 2012; Hauck et al. 2013). In addition, recent measurements of Mercury's tidal response, as expressed in its degree 2 tidal Love number k_2 , yield a value in the range of 0.53–0.57 (Genova et al. 2019; Konopliv et al. 2020), larger than the value of 0.451 reported earlier (Mazarico et al. 2014). This has implications for understanding the likely interior structure of Mercury. We performed an extensive analysis of these different measurements by applying a Markov Chain Monte Carlo (MCMC) analysis. We use the polar and crust–mantle polar moment of inertia, together with a constraint on Mercury's average density. We also either include k_2 as an additional measurement or predict it from our analysis.

We find in our analysis that models that match the lower polar moment value of 0.333 also fit or predict the recent, higher Love number of 0.569, as reported by Genova et al. (2019). When we use the higher polar moment value of 0.346, we cannot simultaneously fit the lower k_2 of 0.451 within the given error bounds. If we use the higher polar moment and predict k_2 , we find an even higher value, 0.63, than the currently reported value range of 0.53–0.57, although the spread in predicted values is also large. This means that the polar moment value of 0.346 is not consistent with the lower k_2 of 0.451, and only marginally consistent with the higher range of k_2 values. This is entirely consistent with the general observation that a higher polar moment results in a larger radius of the core–mantle boundary (CMB) and that a larger CMB radius results in a larger k_2 value (due, in part, to a thinner and thus more flexible crust–mantle shell).

The solid inner core radius in our modeling is a parameter, and not derived from local temperature and pressure. This may result in thermodynamical inconsistencies, and our enforcing of density contrasts at the boundaries should mitigate this. The difference in average density between the solid inner core and the liquid outer core is stable, except when the inner core is large itself. In those cases, for inner core radii that are larger than ~ 0.6 times the CMB radius, the inner core density approaches the liquid densities.

Our results indicate a smaller CMB radius of 1955 ± 20 km, slightly smaller than but still consistent at one standard deviation with the results of Genova et al. (2019). The inclusion of k_2 as a measurement in our MCMC analysis yields results mostly consistent with theirs. The consistency between a lower moment of inertia and higher k_2 can occur for a mantle with lower material strength, even if at the same time a thicker mantle leads to less flexibility.

A recent comprehensive analysis of the implications of the new measurements by Steinbrügge et al. (2021) indicated challenges in matching the new observations, with implications for the structure of the mantle and inner core. They reported the need for low viscosities at the base of the mantle to match the new observations. We also find a wide range of viscosities at the CMB, because lower viscosities match well with higher k_2 values. However, the range of viscosities that we find also includes larger values, and we find trends expected from the modeling (such that higher k_2 values and higher CMB temperatures result in lower CMB viscosities). We also do

not find a strong dependence on grain size. We find that our results are mostly not very sensitive to other parameters in our analysis, such as rigidities, or the thickness or density of the crust.

Steinbrügge et al. (2021) found CMB temperatures around 2100 K, which can be problematic for interior models, as this would imply mantle melting and extended volcanism. Our models do not show that such high CMB temperatures are needed to fit the measurements. If we model the mantle with a constant temperature to mimic a convecting mantle, we find lower CMB temperatures, and we find that the CMB viscosities are higher. However, such a model does not match the polar moment of inertia value as well as the models with a conducting mantle do.

The composition of the core is described by the weight fraction of Si in our analysis. We find relatively small Si weight fractions of 4%–5% for most of our models when we use the measurements of Genova et al. (2019). If we use the higher polar moment value, the weight fraction increases to above 10%. It is often assumed that the weight fractions of Si in the solid and liquid core are the same, but we also performed an analysis where we allowed them to be different, while enforcing a smaller weight fraction in the solid core. We then find the possibility of larger weight fractions of Si in the liquid core, up to $\sim 10\%$, and only a few percent for the solid inner core.

We present several additional parameters that are derived from our interior models, such as values for the inner core temperature and pressure, which are important for the further characterization of Mercury's core. We also include the tidal displacement Love numbers. The radial displacement Love number h_2 was estimated for the first time from MESSENGER altimetry data (Bertone et al. 2021). Their error analysis carefully considered systematic and stochastic effects. Their h_2 value has relatively large error bars, due to limited observability and sensitivity, and due to large correlations with orbit parameters. Our predicted value, $h_2 = 1.02 \pm 0.04$ (one standard deviation, computed from the a posteriori distribution of our MCMC results), is just within their error bounds.

Our analysis did not address the inconsistency between the different obliquity measurements. Additional and combined analysis of both MESSENGER gravity and altimetry may further address this, but that is outside the scope of this analysis. Future data from the BepiColombo mission to Mercury will greatly benefit studies of the planet's interior, by providing improved and additional constraints on the deep interior (e.g., Steinbrügge et al. 2018a; Genova et al. 2021).

The data used in this analysis is provided in previously published work, and the sources are listed in Table 1. The material presented here is partly based upon work supported by NASA under the CRESST II cooperative agreement with award number 80GSFC17M0002 (SG, SB), and partly supported by NASA grant 80NSSC17K0218 (SG). Additional support for this research was provided by NASA's Planetary Science Division Research Program (EM). We thank Laura Lark (Brown University) for discussions. We thank Dr. Yuji Harada and an anonymous reviewer for their comments, which improved this paper. Data figures were generated with the freely available software GMT (Wessel et al. 2013). Colors are chosen from <https://www.ColorBrewer.org> by Cynthia A.

Brewer, Geography, Pennsylvania State University. The scientific color map “roma” (Crameri 2021) is used to prevent visual distortion of the data and the exclusion of readers with color vision deficiencies (Crameri et al. 2020). Additional data files that are the result of this analysis, such as our collection of models from our MCMC analysis, will be available from our data archive, which can be found at <https://pgda.gsfc.nasa.gov/>.

Appendix A

Results from the MCMC Analysis: Additional Figures

We include results from our MCMC analysis of the interior structure of Mercury. We include additional results that show how well we can map the measurements provided by Hauck et al. (2013) and Bertone et al. (2021), in Figure A1, and by Konopliv et al. (2020), in Figure A2.

In the figure set for Figure A3, we show the a posteriori probability density functions from our main analysis using the measurements from Genova et al. (2019). We include distributions for the measurements that we used (A3.1–A3.4), for the parameters that were varied in our analysis (A3.5–A3.15), or those that derived from the resulting models (A3.16–A3.18). We include two additional examples of dependencies between parameters: in Figure A3.19 we show the relationship between the mantle density and weight fraction of Si in the core, and in Figure A3.20 we show the relationship

between the weight fraction of Si in the core and CMB temperature.

We show weight fractions of Si in the core in Figure A4. We use a heat map to indicate clusters in the solutions when plotting the inner core weight fraction versus outer core weight fraction in Figure A4(A). In Figure A4(B), we show the weight fractions for the case where we have separate weight fractions in the inner and outer core, but unlike the results shown in Figure 5, here we limit the weight fraction difference between the inner and outer core to be at most 3% (with the weight fraction in the liquid core always being higher than that of the inner core).

In Figure A5(A), we show how different rheological laws influence the resulting Love number k_2 , and we include a posteriori distributions for k_2 using two different laws in our analysis in Figure A5(B).

In Figure A6, we show results for the CMB temperature and inner core temperature when we expand the CMB temperature bounds from 1600–2000 K to 1200–2400 K.

In Figure A7(A), we show the pressure versus temperature at the ICB, similar to Figure 10, but now color-coded as a heat map, to indicate there are few models with high pressure, a low weight percentage of Si in the core, and low temperature. In Figure A7(B), we show the same pressure–temperature plot as in Figure 10, but with models with weight percentages less than 4% and CMB temperatures less than 1900 K excluded.

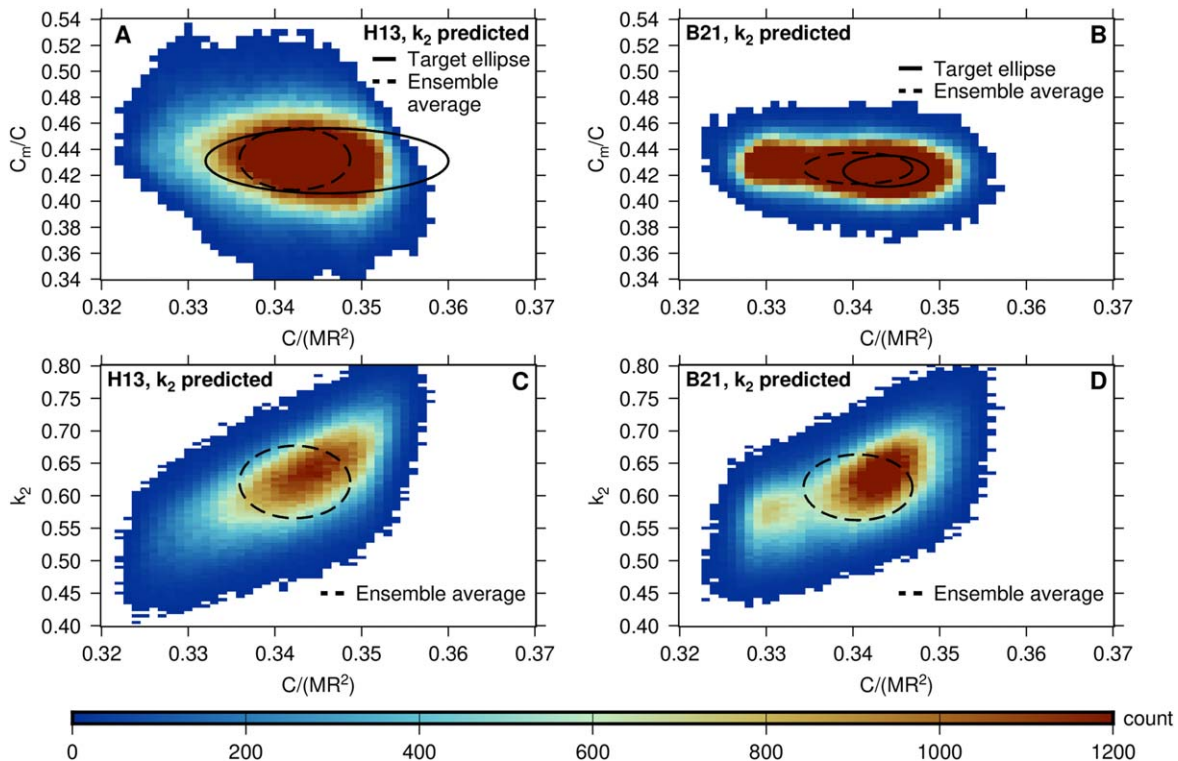


Figure A1. Results from the MCMC analysis, where we plot the polar moment vs. the crust–mantle polar moment (A and B) or the polar moment vs. k_2 (C and D). We use the measurements of $C/(MR^2)$, C_m/C , and average density from Hauck et al. (2013), indicated as H13, or Bertone et al. (2021), indicated as B21. We include ellipses for the measurements (“target”) as well as for the ensemble average. Because neither of these studies estimated k_2 , panels (C) and (D) show the predicted k_2 results, and thus no target ellipse is included.

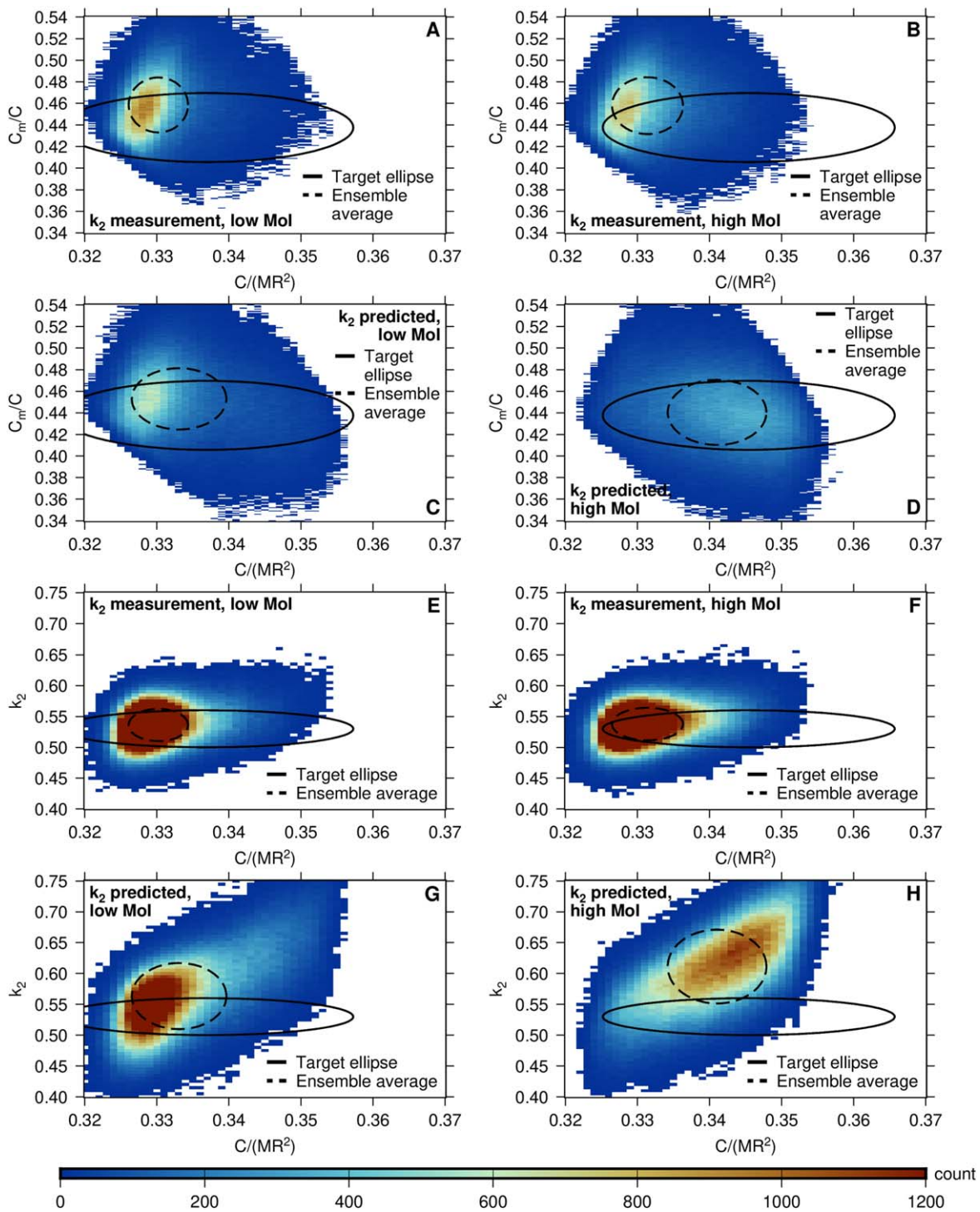


Figure A2. Results from the MCMC analysis, where we plot the polar moment vs. the crust–mantle polar moment (A–D) or the polar moment vs. k_2 (E–H). Here, we use the measurements of Konopliv et al. (2020), where we make a distinction between the reported obliquity values, which result in a lower polar moment of inertia (labeled “low MoI”), and the obliquity derived from the reported pole coordinates, which results in a higher polar moment of inertia (labeled “high MoI”). We make the distinction to illustrate the influence on the mapping of the measurements. We show results for the analysis where we included k_2 as a measurement and where we did not include it, but predicted its value.

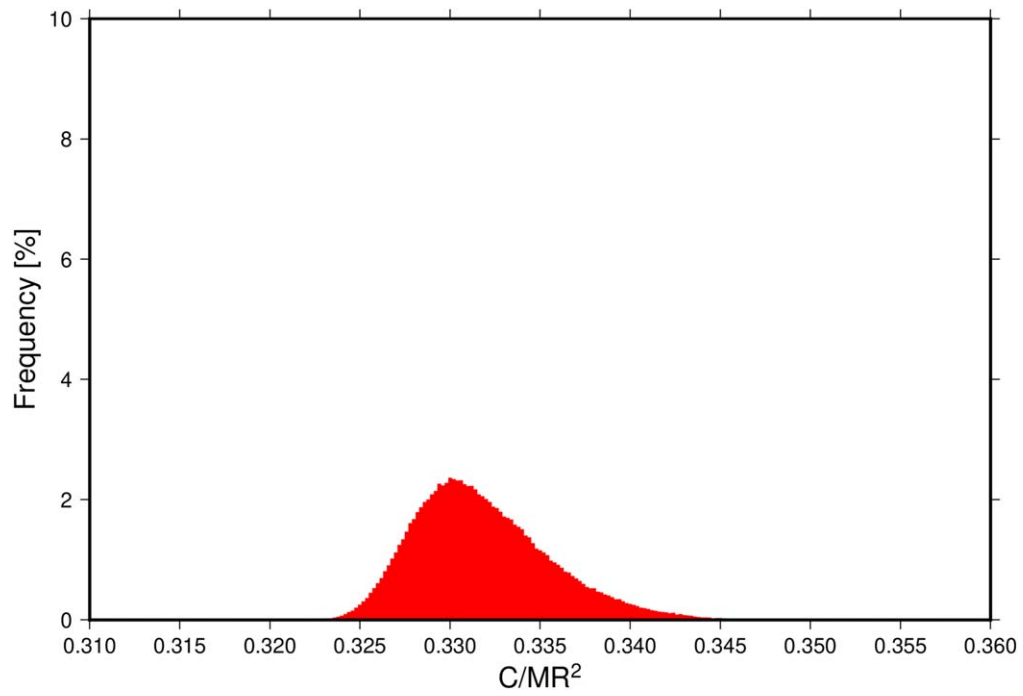


Figure A3. Results of our MCMC analysis using the measurements from Genova et al. (2019) for $C/(MR^2)$. This is a measurement in the analysis. The complete figure set (20 images) is available in the online journal.

(The complete figure set (20 images) is available.)

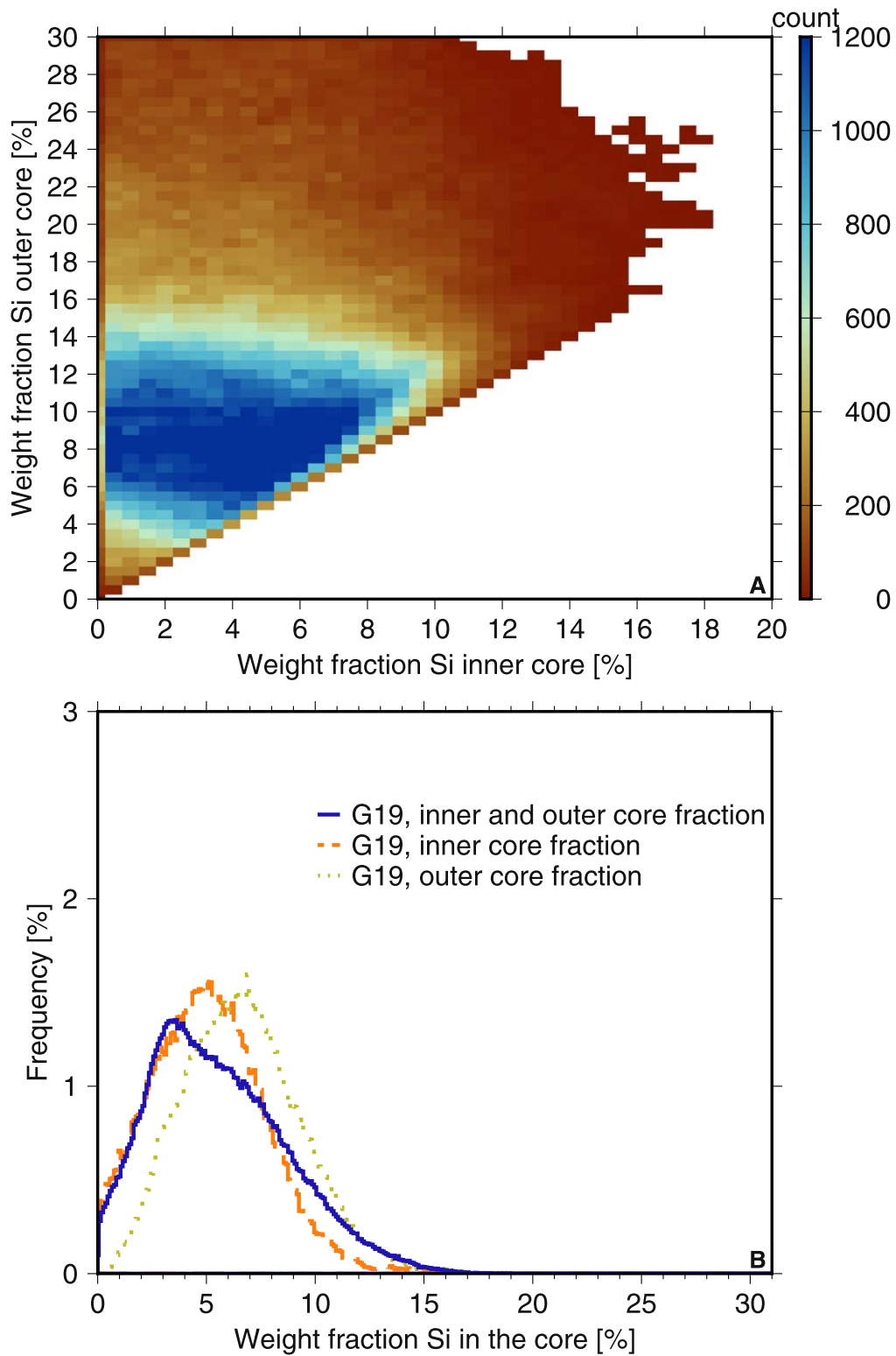


Figure A4. Top (A): inner core weight fraction of Si vs. outer core weight fraction, with the count in bins of 0.5% shown to indicate clusters in the solutions. We used the measurements from Genova et al. (2019), where the weight fractions in the inner core and outer core are different. Bottom (B): weight fractions of Si in the core for the results from the MCMC analysis. We used the measurements from Genova et al. (2019; G19), where we either set the weight fractions of the inner core and outer core to be the same (labeled “inner and outer core fraction”) or separate (indicated by “inner” and “outer”). Here, we limit the difference in weight fraction between the inner and outer core to be at most 3%, as opposed to the results shown in Figure 8, where larger differences were allowed.

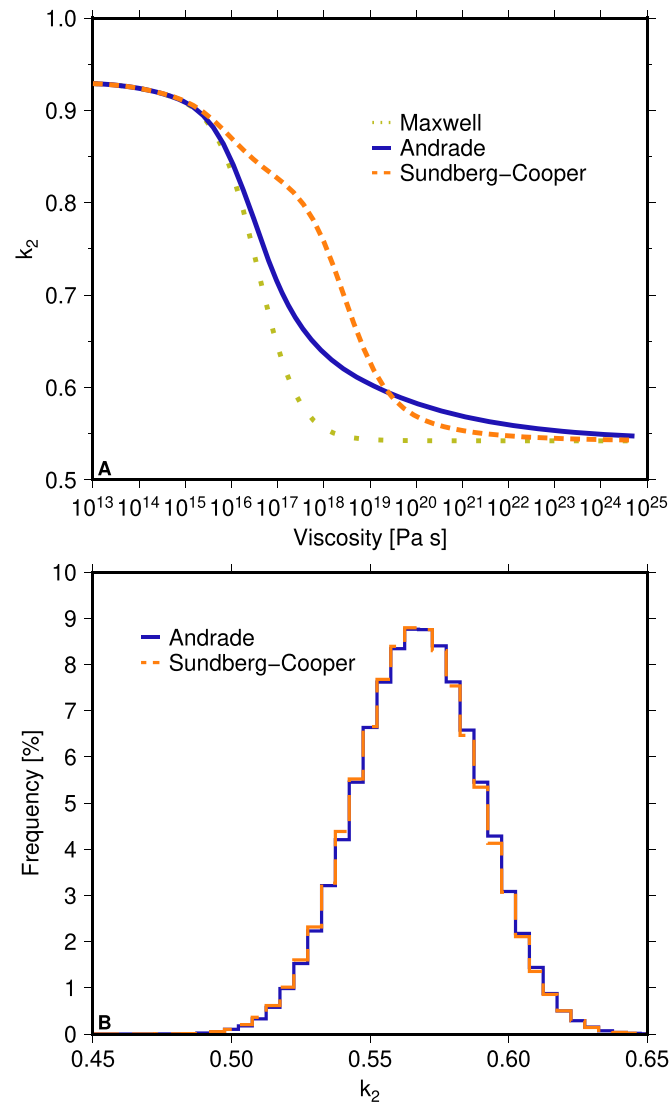


Figure A5. Top (A): viscosity vs. k_2 (which we assume is equal to $|\bar{k}_2| \sim \Re[\bar{k}_2]$) for different rheological laws, showing how different laws can affect k_2 as viscosity varies. For this comparison, we assume a CMB radius of 2020 km, a rigidity of 54 GPa for both crust and mantle, a crustal thickness of 50 km, a core density of 7500 kg m^{-3} , a mantle density of 3200 kg m^{-3} , and a crustal density of 2800 kg m^{-3} . Since we vary the viscosity as a parameter for this comparison, no temperature information is necessary. Bottom (B): results for k_2 from our MCMC analysis when we use the measurements of Genova et al. (2019) with either an Andrade or Sundberg-Cooper rheology. The results are very close, despite possible differences in the viscosity- k_2 relationship, as shown above. We include this merely to illustrate that with the current measurements we cannot distinguish rheological laws.

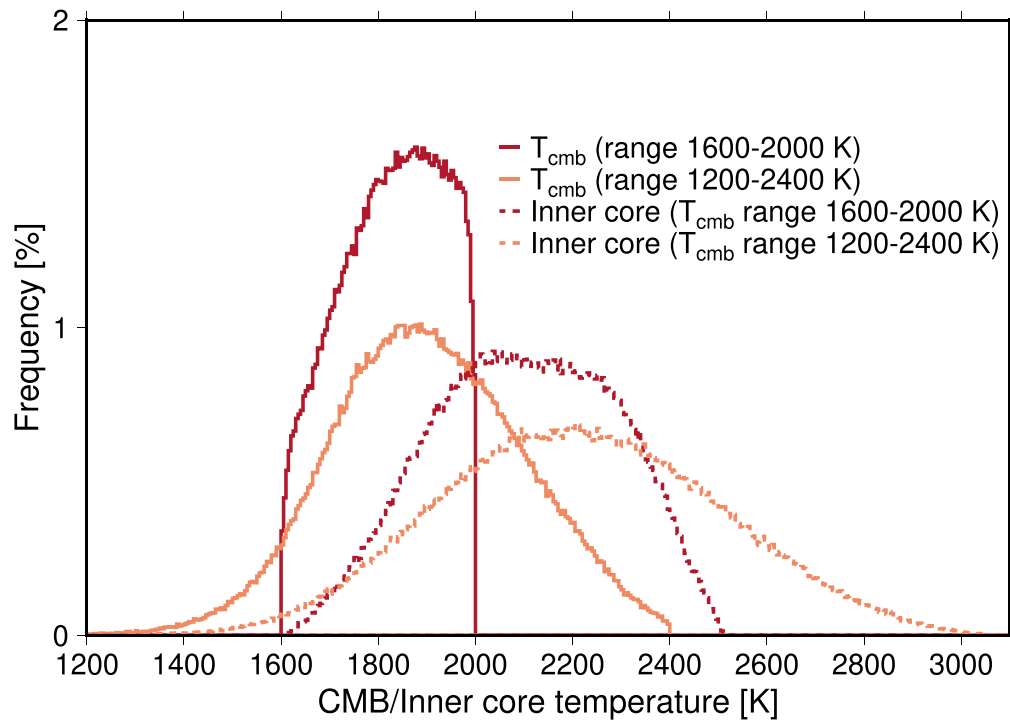


Figure A6. CMB and inner core temperatures for the results from the MCMC analysis using the measurements from Genova et al. (2019), where we expanded the bounds of the CMB temperatures from our original range of 1600–2000 K to 1200–2400 K. The solid lines indicate CMB temperatures and the dashed lines indicate inner core temperatures. While the temperature range increases with the expanded bounds, the results are very similar. We do not find preferences for higher CMB temperatures, for example.

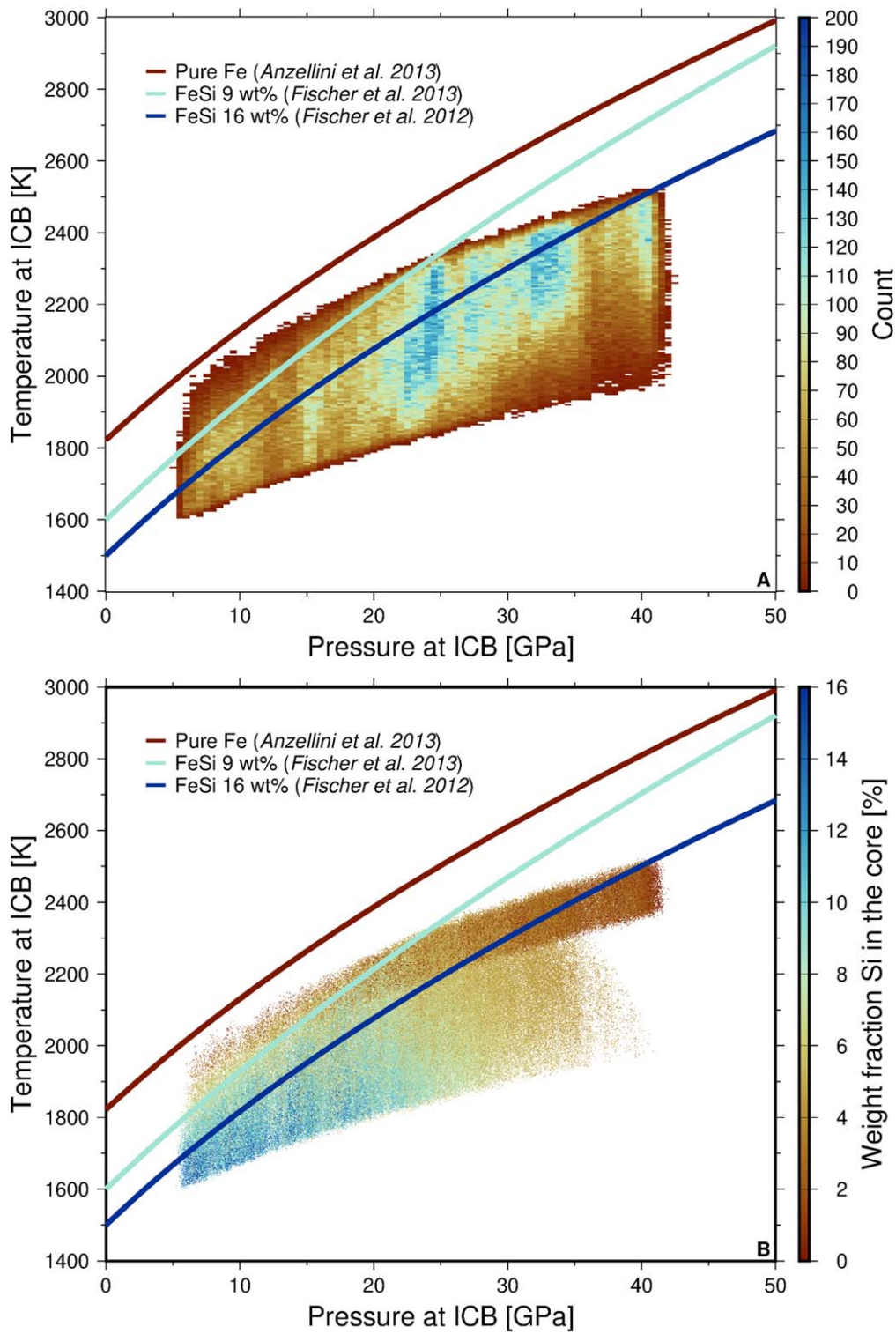


Figure A7. Top (A): similar to Figure 10, this panel shows the pressure at the ICB vs. the temperature of the inner core, this time as a heat map of counts of models within bins. Bottom (B): the same as Figure 10, with models that have weight fractions of Si in the core less than 4% and CMB temperatures less than 1900 K excluded. Melt curves for pure Fe, FeSi at 9 wt% Si, and FeSi at 16 wt% Si are also shown.

ORCID iDs

Sander Goossens  <https://orcid.org/0000-0002-7707-1128>
 Joe P. Renaud  <https://orcid.org/0000-0002-8619-8542>
 Wade G. Henning  <https://orcid.org/0000-0001-9788-2799>
 Erwan Mazarico  <https://orcid.org/0000-0003-3456-427X>
 Stefano Bertone  <https://orcid.org/0000-0001-9885-8440>
 Antonio Genova  <https://orcid.org/0000-0001-5584-492X>

References

- Anderson, J. D., Colombo, G., Esposito, P. B., Lau, E. L., & Trager, G. B. 1987, *Icar*, **71**, 337
- Anderson, W. W., & Ahrens, T. J. 1994, *JGR*, **99**, 4273
- Andrade, E. N. D. C. 1910, *RSPSA*, **84**, 1
- Anzellini, S., Dewaele, A., Mezouar, M., Loubeyre, P., & Morard, G. 2013, *Sci*, **340**, 464
- Asanuma, H., Ohtani, E., Sakai, T., et al. 2010, *PCM*, **37**, 353
- Bagheri, A., Khan, A., Al-Attar, D., Crawford, O., & Giardini, D. 2019, *JGRE*, **124**, 2703
- Baland, R.-M., Yseboodt, M., Rivoldini, A., & Van Hoolst, T. 2017, *Icar*, **291**, 136
- Balog, P. S., Secco, R. A., Rubie, D. C., & Frost, D. J. 2003, *JGRB*, **108**, 2124
- Bertone, S., Mazarico, E., Barker, M. K., et al. 2021, *JGRE*, **126**, e06683
- Beutl, M., Potlacher, G., & Jäger, H. 1994, *IJT*, **15**, 1323
- Boujibar, A., Goossens, S., Nittler, L. R., & Richter, K. 2021, MEXAG (Mercury Exploration Assessment Group) Meeting [#6035], https://www.hou.usra.edu/meetings/mexag2021/pdf/mexag2021_program.htm
- Byrne, P. K., Klimczak, C., Şengör, A. M. C., et al. 2014, *NatGe*, **7**, 301
- Cartier, C., Namur, O., Nittler, L. R., et al. 2020, *E&PSL*, **534**, 116108
- Cavanaugh, J. F., Smith, J. C., Sun, X., et al. 2007, *SSRv*, **131**, 451
- Chabot, N. L., Wollack, E. A., Klima, R. L., & Minitti, M. E. 2014, *E&PSL*, **390**, 199
- Chapman, C. R. 1988, in *Mercury*, ed. F. Vilas, C. R. Chapman, & M. S. Matthews (Tucson, AZ: Univ. Arizona Press), 1
- Colombo, G. 1966, *AJ*, **71**, 891
- Cramer, F. 2021, Scientific Colour Maps, 7.0.0, Zenodo, doi:10.5281/zenodo.1243862
- Cramer, F., Shephard, G. E., & Heron, P. J. 2020, *NatCo*, **11**, 5444
- Dumberry, M. 2021, *JGRE*, **126**, e06621
- Dumberry, M., & Rivoldini, A. 2015, *Icar*, **248**, 254
- Dunne, J. A. 1974, *Sci*, **185**, 141
- Efroimsky, M. 2012, *ApJ*, **746**, 150
- Ernst, C. M., Chabot, N. L., Klima, R. L., et al. 2021, *LPSC*, **52**, 2565
- Fischer, R. A., Campbell, A. J., Caracas, R., et al. 2012, *E&PSL*, **357**, 268
- Fischer, R. A., Campbell, A. J., Caracas, R., et al. 2014, *JGRB*, **119**, 2810
- Fischer, R. A., Campbell, A. J., Reaman, D. M., et al. 2013, *E&PSL*, **373**, 54
- Genova, A., Goossens, S., Mazarico, E., et al. 2019, *GeoRL*, **46**, 3625
- Genova, A., Hussmann, H., Van Hoolst, T., et al. 2021, *SSRv*, **217**, 31
- Genova, A., Mazarico, E., Goossens, S., et al. 2018, *NatCo*, **9**, 289
- Hastings, W. K. 1970, *Biometrika*, **57**, 97
- Hauck, S. A., Margot, J.-L., Solomon, S. C., et al. 2013, *JGRE*, **118**, 1204
- Hauck, S. A., Solomon, S. C., & Smith, D. A. 2007, *GeoRL*, **34**, L18201
- Henning, W. G., & Hurford, T. 2014, *ApJ*, **789**, 30
- Henning, W. G., O'Connell, R. J., & Sasselov, D. D. 2009, *ApJ*, **707**, 1000
- Jackson, I., Faul, U. H., Fitz Gerald, J. D., & Tan, B. H. 2004, *JGRB*, **109**, B06201
- Jackson, I., Faul, U. H., Suetsugu, D., et al. 2010, *PEPI*, **183**, 151
- Jackson, I., Gerald, F., John, D., Faul, U. H., & Tan, B. H. 2002, *JGRB*, **107**, 2360
- Jara-Orue, H. M. 2016, PhD thesis, Delft Univ. of Technology, <https://doi.org/10.4233/uuid:2e35b789-735a-47a3-ac4f-63dd7651de44>
- Johnson, C. L., Philpott, L. C., Anderson, B. J., et al. 2016, *GeoRL*, **43**, 2436
- Katsura, T., Shimizu, H., Momoki, N., & Toh, H. 2021, *JGR*, **354**, 114112
- Knibbe, J. S., Rivoldini, A., Luginbuhl, S. M., et al. 2021, *JGRE*, **126**, e06651
- Knibbe, J. S., & van Westrenen, W. 2015, *JGRE*, **120**, 1904
- Knibbe, J. S., & van Westrenen, W. 2018, *E&PSL*, **482**, 147
- Komabayashi, T., & Fei, Y. 2010, *JGRB*, **115**, B03202
- Konopliv, A. S., Park, R. S., & Ermakov, A. I. 2020, *Icar*, **335**, 113386
- Kuwayama, Y., & Hirose, K. 2004, *AmMin*, **89**, 273
- Lin, J.-F., Campbell, A. J., Heinz, D. L., & Shen, G. 2003, *JGRB*, **108**, 2045
- Malavergne, V., Toplis, M. J., Berthet, S., & Jones, J. 2010, *Icar*, **206**, 199
- Margot, J., Padovan, S., Peale, S. J., & Solomon, S. C. 2011, *AGUFM*, **2011**, P44B-01
- Margot, J.-L., Hauck, S. A., II, Mazarico, E., Padovan, S., & Peale, S. J. 2018, in *Mercury-The View after MESSENGER*, ed. S. C. Solomon, L. R. Nittler, & B. J. Anderson (Cambridge: Cambridge Univ. Press), 85
- Margot, J.-L., Peale, S., Solomon, S., et al. 2012, *JGRE*, **117**, E00L09
- Margot, J.-L., Peale, S. J., Jurgens, R. F., Slade, M. A., & Holin, I. V. 2007, *Sci*, **316**, 710
- Mazarico, E., Genova, A., Goossens, S., et al. 2014, *JGRE*, **119**, 2417
- Metropolis, N., Rosenbluth, A. W., Rosenbluth, M. N., Teller, A. H., & Teller, E. 1953, *JChPh*, **21**, 1087
- Michel, N. C., Hauck, S. A., Solomon, S. C., et al. 2013, *JGRE*, **118**, 1033
- Morard, G., Andrault, D., Antonangeli, D., & Bouchet, J. 2014, *CRGeo*, **346**, 130
- More, J., Sorenson, D., Garbow, B., & Hillstrom, K. 1984, in *Sources and Development of Mathematical Software*, ed. W. Cowell (Upper Saddle River, NJ: Prentice-Hall), 88
- Mosegaard, K., & Tarantola, A. 1995, *JGR*, **100**, 12431
- Ness, N. F., Behannon, K. W., Lepping, R. P., Whang, Y. C., & Schatten, K. H. 1974, *Sci*, **185**, 151
- Ozawa, H., Hirose, K., Yonemitsu, K., & Ohishi, Y. 2016, *E&PSL*, **456**, 47
- Padovan, S., Margot, J.-L., Hauck, S. A., Moore, W. B., & Solomon, S. C. 2014, *JGRE*, **119**, 850
- Peale, S. J. 1969, *AJ*, **74**, 483
- Peale, S. J. 1976, *Natur*, **262**, 765
- Peale, S. J., Margot, J.-L., Hauck, S. A., & Solomon, S. C. 2016, *Icar*, **264**, 443
- Peale, S. J., Phillips, R. J., Smith, D. E., & Zuber, M. T. 2002, *M&PS*, **37**, 1269
- Peltier, W. R. 1974, *RvGSP*, **12**, 649
- Peplowski, P. N., Evans, L. G., Hauck, S. A., et al. 2011, *Sci*, **333**, 1850
- Renaud, J., & Henning, W. 2018, *ApJ*, **857**, 98
- Rivoldini, A., & van Hoolst, T. 2013, *E&PSL*, **377**, 62
- Rivoldini, A., Van Hoolst, T., & Verhoeven, O. 2009, *Icar*, **201**, 12
- Sakairi, T., Ohtani, E., Kamada, S., et al. 2017, *PEPS*, **4**, 10
- Sanloup, C., Fiquet, G., Gregoryanz, E., Morard, G., & Mezouar, M. 2004, *GeoRL*, **31**, L07604
- Smith, D. E., Zuber, M. T., Phillips, R. J., et al. 2012, *Sci*, **336**, 214
- Sohl, F., & Schubert, G. 2015, in *Treatise on Geophysics*, ed. G. Schubert (2nd edn.; Oxford: Elsevier), 23
- Solomon, S. C., McNutt, R. L., Gold, R. E., & Domingue, D. L. 2007, *SSRv*, **131**, 3
- Spada, G. 2008, *CG*, **34**, 667
- Stark, A., Oberst, J., Preusker, F., et al. 2015, *GeoRL*, **42**, 7881
- Steinbrügge, G., Dumberry, M., Rivoldini, A., et al. 2021, *GeoRL*, **48**, e89895
- Steinbrügge, G., Padovan, S., Hussmann, H., et al. 2018a, *JGRE*, **123**, 2760
- Steinbrügge, G., Stark, A., Hussmann, H., Wickhusen, K., & Oberst, J. 2018b, *P&SS*, **159**, 84
- Sundberg, M., & Cooper, R. F. 2010, *PMag*, **90**, 2817
- Tao, R., & Fei, Y. 2021, *E&PSL*, **562**, 116849
- Thomas, N., Hussmann, H., Spohn, T., et al. 2021, *SSRv*, **217**, 25
- Thor, R. N., Kallenbach, R., Christensen, U. R., et al. 2020, *A&A*, **633**, A85
- Tiesinga, E., Mohr, P., Newell, D., & Taylor, B. 2020, The 2018 CODATA Recommended Values of the Fundamental Physical Constants (Web Version 8.1), Gaithersburg, MD: NIST, <http://physics.nist.gov/constants>
- Tosi, N., Grott, M., Plesa, A.-C., & Breuer, D. 2013, *JGRE*, **118**, 2474
- Turcotte, D. L., & Schubert, G. 2002, *Geodynamics* (Cambridge: Cambridge Univ. Press)
- Verma, A. K., & Margot, J.-L. 2016, *JGRE*, **121**, 1627
- Wardinski, I., Langlais, B., & Thébault, E. 2019, *JGRE*, **124**, 2178
- Wessel, P., Smith, W. H. F., Scharroo, R., Luis, J., & Wobbe, F. 2013, *EOSTr*, **94**, 409
- Yu, X., & Secco, R. 2008, *HPR*, **28**, 19